



HAL
open science

Integrated geological-geophysical investigation of gold-hosting Rhyacian intrusions (Yaou, French Guiana), from deposit-to district-scale

Vincent Combes, Aurélien Eglinger, Anne-Sylvie André-Mayer, Yoram Teitler, Mark Jessell, Armin Zeh, Laurie Reisberg, Arnauld Heuret, Pierre Gibert

► To cite this version:

Vincent Combes, Aurélien Eglinger, Anne-Sylvie André-Mayer, Yoram Teitler, Mark Jessell, et al.. Integrated geological-geophysical investigation of gold-hosting Rhyacian intrusions (Yaou, French Guiana), from deposit-to district-scale. *Journal of South American Earth Sciences*, 2022, 114, pp.103708. 10.1016/j.jsames.2021.103708 . insu-03661246

HAL Id: insu-03661246

<https://insu.hal.science/insu-03661246>

Submitted on 8 Jan 2024

HAL is a multi-disciplinary open access archive for the deposit and dissemination of scientific research documents, whether they are published or not. The documents may come from teaching and research institutions in France or abroad, or from public or private research centers.

L'archive ouverte pluridisciplinaire **HAL**, est destinée au dépôt et à la diffusion de documents scientifiques de niveau recherche, publiés ou non, émanant des établissements d'enseignement et de recherche français ou étrangers, des laboratoires publics ou privés.



Distributed under a Creative Commons Attribution - NonCommercial 4.0 International License

1 **Integrated geological-geophysical investigation of gold-hosting Rhyacian** 2 **intrusions (Yaou, French Guiana), from deposit- to district-scale**

3
4 Vincent Combes^{1, 2, *}, Aurélien Eglinger¹, Anne-Sylvie Andre-Mayer¹, Yoram Teitler¹, Mark
5 Jessell³, Armin Zeh⁴, Laurie Reisberg⁵, Arnauld Heuret⁶, Pierre Gibert²

6
7 ¹Université de Lorraine-CNRS, CREGU, laboratoire GeoRessources, 54500 Nancy, France

8 ²AMG, Auplata Mining Group, ZI Dégrad des Cannes, 97354, Rémire Montjoly, France

9 ³University of Western Australia, CET, 35 Stirling Highway, 6009 Crawley, Australia

10 ⁴Karlsruher Institut für Technologie (KIT), 76131 Karlsruhe, Germany

11 ⁵Centre de Recherches Pétrographiques et Géochimiques (CRPG), UMR 7358 CNRS-Université de Lorraine, BP
12 20, 54501 Vandoeuvre-lès-Nancy Cedex, France

13 ⁶Université de Guyane / Géosciences Montpellier (UMR 5243), 97300 Cayenne, France

14
15
16 *corresponding author (vincent.combes@univ-lorraine.fr)

17 18 19 **Abstract**

20
21 The mineral system concept, which combines integrated information from all kinds of
22 geological and geophysical studies, is a very useful approach to predict and locate structures
23 and lithologies potentially associated with gold mineralization at all scales (i.e., upscaling from
24 craton- to district- to camp- to deposit-scale). This is demonstrated in this study where the Yaou
25 deposit, located in French Guiana within Rhyacian terranes, formed and deformed during the
26 Trans-Amazonian orogenic cycle (ca. 2600-1950 Ma), is used as a case study. The deposit
27 comprises numerous intrusions hosting the bulk of the high-grade gold mineralization at Yaou,
28 associated with a quartz-carbonate veining system. Both intrusive and gold events are dated in
29 order to constrain Yaou in the regional litho-structural framework. Spatially associated with the
30 Central Yaou Shear Zone (CYSZ), one of the quartz monzodiorite yields a U-Pb zircon age of
31 2131 ± 6 Ma, supra-chondritic ϵ_{Hf} of ca. 2.5, and Hf model ages at ca. 2.6-2.4 Ga. These data
32 suggest Paleoproterozoic rock formation due to reworking of juvenile crust, derived from the
33 depleted mantle during the late Archean to early Paleoproterozoic. The main and economic gold
34 event hosted by the quartz monzodiorite is dated at 2105 ± 25 Ma by Re-Os isotope analyses of
35 Au-bearing pyrite, representing the first date for gold mineralization in French Guiana. A multi-
36 scale approach using airborne magnetic and radiometric data allows to better understand the

37 spatial distribution of the intrusions and possibly associated shear zones, both related to gold
38 mineralization events. The intrusions and associated shear zones are interpreted as being
39 parallel along a N60° trend and replicated laterally toward the northwest. A temporal
40 association is defined between the shearing deformation and the magmatic event, both being
41 synchronous with a possibility of pre-shearing intrusion and a protracted magmatic phase active
42 while shearing. The Yaou-type intrusion-hosted mineralization can be targeted along these
43 N60°-striking structures. This integrated approach opens some targeting options, previously
44 unrecognized within the southern Paramaca Greenstone Belt.

45

46

47 **Keywords:** Mineral system, intrusion-hosted gold, Re-Os geochronology, Structural patterns,
48 geophysics, Guiana Shield

49

50

51 **1. Introduction**

52

53 Ore deposits are generated from a variety of natural processes, from lithospheric to nanoscale,
54 that concentrate elements into a small volume that can be economically mined (Jenkin et al.
55 2015). Mineral deposits are by definition geographically small in extent compared to surface
56 area and thickness of the crust, even if they result from geological and geodynamic processes
57 that occur, and can be mapped, at a variety of larger scales (McCuaig et al., 2010; Hronsky et
58 al., 2012). Ore mobilization, transfer and deposition are linked to geological processes leading
59 to the concept of mineral systems, which encompasses “*all geological factors that control the*
60 *generation and preservation of mineral deposits*” (Wyborn et al., 1994; McCuaig and Hronsky,
61 2014 and references therein). Although there are a variety of interpretations of what a mineral
62 system is (e.g., Wyborn et al. 1994; McCuaig et al., 2010; Huston et al. 2012), most include
63 factors such as the geological setting, the timing and duration of deposition, the source(s) and
64 nature of mineralising fluids (including melts), the pathways used by the respective fluids and
65 fluid flow drivers, the depositional site, mechanisms of metal transport and deposition, and
66 post-depositional modifications. Unravelling the structural and lithological settings of a gold

67 deposit at various scale, from ore shoot to metallogenic province, is thus a key to understand
68 the mineral system and enhancing exploration targeting.

69

70 For regional exploration, an understanding of mineral systems is important when zooming in
71 from (1) province-scale (connection between lithospheric processes and metal endowment by
72 studying plumbing structures as discussed by Bierlein et al. (2006, 2009), Begg et al. (2010),
73 Hronsky et al. (2012), and Motta et al. (2019)); to (2) district-scale architecture of structural
74 networks (Siddorn et al., 2020). This scalability in mineral exploration requires the integration
75 of a large set of geophysical, geological and geochemical data (Niiranen et al., 2019; Nykänen
76 et al., 2017). Working both on the structural and lithological framework combining geological
77 (structural geology, geochemistry, and geochronology) and geophysical (magnetometry,
78 gamma-ray spectrometry, remote sensing, and gravimetry) techniques, in accordance with 3D
79 models of Au deposits at the camp-scale, will deliver insights on the deposit to district-scale of
80 such mineral system.

81

82 Integration of regional geological and geophysical datasets is particularly useful in tropical
83 regions where orebodies are commonly covered by dense vegetation and/or thick lateritic
84 profiles such as on the Guiana Shield in South America or on the West African Craton. For
85 such regions, integrated studies can provide deep insights into both (1) the lithospheric
86 architecture and (2) the structural-metamorphic-magmatic evolution and related (gold)
87 mineralization events. Such an intergraded approach has been carried out recently on the West
88 African Craton, by deciphering litho-structural patterns such as shear zone geometries and
89 kinematics (Metelka et al., 2011; Jessell et al., 2016; Chardon et al., 2020), and their link to the
90 distribution of gold deposits (Perrouy et al., 2012; Baratoux et al., 2015). On the Amazon
91 Craton, it has been applied to unravel the lithosphere geometry of copper and gold
92 mineralization systems using satellite gravimetry, airborne potential field data (gravimetry and
93 geomagnetics), combined with information from passive seismic (wave speeds to constrain
94 crustal and lithospheric thickness), geochronological, and isotope-geochemical data (Nd model
95 ages, mineral crystallisation ages, Nd isotope ratios) - (Motta et al., 2019).

96

97 This study will develop a similar approach in the Guiana Shield, focusing on the Yaou district
98 located in French Guiana (Fig. 1). The Yaou gold deposit displays a polyphase gold
99 mineralization where the main orebodies are defined as intrusion-hosted along the Central Yaou
100 Shear Zone (CYSZ), (Milesi et al., 2003, Eglinger et al., 2020; Combes et al., 2021a). While a
101 first gold system related to the shearing of a pyrite-rich metasedimentary unit is observed
102 (Combes et al., 2021a), most of the high-grade mineralization is associated with one set of
103 hydrothermal quartz-calcite veins formed during the brittle D_{4YA} deformation phase. A strong
104 rheological controlled is demonstrated for the ore shoots, localized mostly within the intrusions.
105 Yaou is a typical undercover deposit with its dense Amazonian Forest and thick lateritic profiles
106 (Théveniaut & Freyssinet, 2002), representing a suitable ground for the application of such an
107 integrated geological and geophysical approach

108 New geological data (geochemistry, Lu-Hf isotopy and zircon U-Pb) for the Yaou quartz
109 monzodiorite hosting the main economic gold vein system (dated here using the Re-Os
110 geochronometer on pyrite) will allow time correlation within the Trans-Amazonian orogenic
111 evolution. New district-, camp- and deposit-scale structural and lithological maps based on
112 airborne geophysical data including airborne magnetometry and radiometry (Th, U and K), will
113 help to define the relation between shearing, magmatism, and gold mineralization. All
114 geological and geophysical data are integrated in a 4D model and discussed together, with the
115 aim to target new gold deposits in the otherwise poorly exposed region. The results will help to
116 improve mineral exploration strategies in French Guiana and in the whole Guiana Shield.

117

118

119 **2. Geological background**

120

121 ***2.1. Regional geology***

122

123 The Guiana Shield, with at the south the Guapore Shield, and at the east its counterpart, the Leo
124 Man craton in West Africa (Fig. 1), is spatially and temporally associated with the Trans-
125 Amazonian orogenic cycle (ca. 2600-1950 Ma), (Delor et al., 2003a, b; Enjolvy, 2008;
126 Kroonenberg et al., 2016) which is characterized by a period of crustal growth followed by a
127 crustal reworking phase (Vanderhaeghe et al., 1998).

128

129 Regarding main formations identified within the Guiana Shield, Archean terranes referred to as
130 the Imataca Complex in Venezuela and the Amapá Block in Brazil (Gibbs and Barron, 1993)
131 are present along with Rhyacian volcano-sedimentary formations (greenstone belts), TTG-like
132 complexes, late high-K calc-alkaline intrusions, and late Rhyacian high grade belt (see Fig. 1
133 and synthesis by Kroonenberg et al., 2016 and references therein).

134 While moving from an oceanic-arc environment to an intracratonic basin environment, the
135 tectonic framework established by Ledru et al. (1991), Gibbs and Barron (1993) and updated
136 by Vanderhaeghe et al. (1998), Delor et al. (2003a, b), Enjolvy (2008), and Kroonenberg et al.
137 (2016) defines an early D₁ phase, associated with a compressional regime in a convergent
138 context. Vanderhaeghe et al. (1998) proposed a subduction model favored by (i) the calc-
139 alkaline geochemical signature of the plutonic-volcanic intrusions; (ii) deformation recorded
140 by the turbidites which is comparable to the deformation recorded in modern accretionary
141 prisms and (iii) the *HP-LT* (high pressure-low temperature) metamorphism recorded by the
142 sediments of the Upper Detrital Unit. This D₁ phase, dated at ca. 2180-2130 Ma, produced
143 TTG-type intrusions and volcanosedimentary formations within an oceanic volcanic arc or
144 back-arc environment (Vanderhaeghe et al., 1998; Delor et al., 2003b). A N-S convergence is
145 proposed for this early phase. The following D_{2a} phase (ca. 2110-2080 Ma) in a collisional
146 context and ending of subduction is marked by trans-tension and sinistral sliding together with
147 folding of the volcano-sedimentary formation (Vanderhaeghe et al., 1998; Delor et al., 2003a,
148 b). The North Guiana Trough (NGT) shear zone (Fig. 1 and 2) (Egal et al., 1991) is formed
149 during this deformation phase (Ledru et al., 1991, Vanderhaeghe et al., 1998). The D_{2b}
150 deformation phase dated at ca. 2070-2060 Ma (Delor et al., 2003a, b) is responsible for dextral
151 strike slip shearing (Vanderhaeghe et al., 1998; Delor et al., 2003b) together with a crustal
152 stretching. Regarding kinematic directions, a northeast-southwest convergence for D_{2a} is
153 proposed by Delor et al. (2003a, b). Delor et al. (2003b) define a late D_{2c} phase associated with
154 granulite facies metamorphism which is currently not present in French Guiana and dated at ca.
155 2110-1990 Ma (DeRoever et al., 2003; Klaver et al., 2015).

156

157 From the GIS-based lithological map of the BRGM, a simplified geological map of French
158 Guiana is produced for this study (Fig. 2) where all dating information is from Delor et al.
159 (2003a, b and references therein).

160

161 The oldest basement complex in French Guiana, the « Ile de Cayenne » has an age of ca. 2216-
162 2208 Ma based on dating of two suites, an amphibolite/gabbroic and a trondhjemite. Later, a
163 first generation of TTG-like (dated at ca. 2183-2155 Ma) was emplaced both in the northern
164 part and in the south of French Guiana (Fig. 2). The Central TTG-like complex, situated in the
165 central part of French Guiana between the two east-west greenstone belts is composed of a
166 granodioritic gneiss unit (dated at ca. 2152-2144 Ma) and undifferentiated TTG dated at ca.
167 2140-2120 Ma which are also encountered in the northern part of French Guiana. Minor mafic
168 to ultramafic complexes are identified and dated at ca. 2149-2135 and ca. 2093-2090 Ma. A
169 granitic suite dated at ca. 2105-2090 Ma is mostly displayed at the south and central east parts
170 of the region (Fig. 2) followed by late Rhyacian units defined as peraluminous leucogranites
171 (ca. 2092-2078 Ma) and late metaluminous plutonism (ca. 2069-2060 Ma). Apart from
172 plutonism, the main units include the Lower volcanic and sedimentary unit (Paramaca
173 greenstone belt) with its two east-west belts (Fig. 2) where all gold occurrences are currently
174 known (Milesi et al., 2003) and the D_{2a}-related Upper Detrital Unit associated with pull-apart
175 basins composed of pelites, sandstones and conglomerates. Post-Trans-Amazonian units
176 include mafic dikes (dolerites dated at ca. 1900-1800 Ma, ca. 808 Ma and ca. 198-189 Ma) and
177 Quaternary sediments, mostly mapped in the northern part of French Guiana, along the Atlantic
178 coast (Fig. 2).

179

180 ***2.2. Geological features at the district-scale***

181

182 In the Yaou district, several gold occurrences are known from a 50-60 km wide radius around
183 the Yaou camp (Fig. 3), such as Dorlin, Bois Blanc, Chaina, and Tomantoni (among others).
184 Each gold occurrence is hosted either within metasedimentary or metavolcanic rock units of the
185 southern PGB (Paramaca Greenstone Belt). According to the latest geological map of Delor et
186 al. (2003b), which is based on historical BRGM surveys and airborne geophysical
187 interpretations (Fig. 3), the Yaou district consists mainly of metavolcanic rocks locally
188 intercalated by metasedimentary rocks, in particular in its eastern and western parts. This
189 volcano-sedimentary succession was intruded by granodiorite at ca. 2152-2144 Ma, and
190 subsequently by tonalite-trondhjemite-granodiorite (TTG) at ca. 2140-2120 Ma, and finally by
191 a Neoproterozoic dolerite dike at ca. 808 Ma (Delor et al., 2003b). The dolerite dike strikes
192 N165° and crosscuts the western part of the Yaou deposit. The CYSZ is located within the PGB,
193 at the border with the eastern TTG-like complex. Regional structures, drawn mostly from

194 aeromagnetic interpretations, strike northwest-southeast, east-west and north northeast-south
195 southwest (Fig. 3).

196

197 *2.2.3. Intrusion and deformation features at the camp- and deposit-scale*

198

199 At the deposit- to the camp-scale, a multiphase deformation model has been established
200 (Combes et al., 2021a). Considering all mineralized bodies within the central part of the Yaou
201 deposit, a model is presented in Figure 4 where quartz monzodiorite bodies are aligned along
202 the sinistral CYSZ. The linear array of intrusions, parallel to the CYSZ, can be traced for more
203 than 4.5 km along strike (Combes et al., 2021a). The intrusions show a great range of wide,
204 from a few meters up to 80 m in the central part of the deposit. The ductile $D_{1/2YA}$ phase is
205 responsible for the main penetrative foliation (S_2 striking $N90^\circ$ - $N120^\circ$ with a subvertical dip)
206 while the D_{3YA} phase is related to shearing (sinistral CYSZ; $N60^\circ$, 70° NW; Fig. 4). An intrusive
207 quartz monzodiorite event is identified as being pre- to syn- D_{3YA} . The following phase D_{4YA}
208 represents a brittle quartz-carbonate veining set hosted preferentially within intrusive bodies
209 and along the shear zone. A strong rheological control is interpreted for this main auriferous
210 event (see Combes et al., 2021a). The D_{5YA} brecciation event locally affects the D_{4YA} vein
211 system. These deformation phases are not precisely correlated to the petro-structural framework
212 established by Delor et al. (2003b) for the whole region before the present study. The dominant
213 host lithology at Yaou consists of a fine-grained, strongly schistosed and locally folded unit,
214 characterized by a dark greenish chloritic alteration referred to as metavolcanite. Locally, a
215 fine-grained, greyish to brownish, laminated and strongly schistosed metasediment is also
216 observed, displaying a primary bedding and millimetric stretched lithic clasts of quartz and
217 plagioclase. Both units belong to the Lower volcanic and sedimentary formation of the
218 Paramaca Greenstone Belt (Milesi et al., 2003).

219

220 With over 36 000 m drilled at Yaou (auger, RC and diamond drilling; AMG exploration
221 database) a precise modeling of the central part of the deposit has been drawn at the camp-scale.
222 A Leapfrog Geo view (north northwest -south southeast) of the model is presented on Figure 5
223 using assay data, where the D_{3YA} sinistral shear zone correlates with the $N60^\circ$ striking
224 $Au_{D0/D3/D4YA}$ orebodies whereas the bulk of the Au_{D4YA} orebodies are located within the quartz
225 monzodiorite bodies giving two subparallel ore trends striking $N60^\circ$.

226 When zooming out from the camp-scale to the district-scale, no detailed interpretation has been
227 made prior to this study, as no outcrop was found for this work, so no lineation was measured,
228 and no far-field stress established. The only data available are the geophysical survey and their
229 interpretation as historical gold in soil surveys (AMG) do not help at the district-scale.

230

231 **3. Methodology and data use**

232

233 ***3.1. Whole-rock analyses of trace and major elements***

234

235 Whole-rock analyses of trace and major elements (Table 1) were conducted on 20 cm-long half-
236 drillcore samples at the SARM (Service d'Analyses des Roches et des Minéraux) laboratory
237 (CRPG, Centre de Recherches Pétrographiques et Géochimiques) in Nancy, France, following
238 Carignan et al. (2001). Veins and unfresh pieces were removed prior to crushing and
239 pulverization at the GeoRessources laboratory (Nancy, France). Trace elements were analysed
240 by inductively coupled plasma mass spectrometry (ICP-MS) and oxides were analysed by
241 inductively coupled plasma optical emission spectrometry (ICP-OES). Results are presented
242 here for the five least altered samples out of twelve sampled cores after careful petrographic
243 studies of hydrothermal alteration mineralogy.

244

245 ***3.2. U-Pb dating and Lu-Hf isotope analyses of zircon***

246

247 Zircon grains were separated from ca. 30 kg of quartz monzodiorite saprock powdered with a
248 jaw crusher and a roller mill at the CRPG in Nancy (France) and concentrated using a Gemini
249 shaker table, followed by heavy liquids (diiodomethane: density = 3.31 g/cm³) and a Frantz
250 isodynamic magnetic separator. Individual grains were then handpicked, mounted in epoxy
251 blocks, and polished to expose their cores. Prior to *in-situ* isotope analyses the internal textures
252 of the zircon grains were characterised by means of cathodoluminescence (CL) and back
253 scattered electron (BSE) imaging performed with a TESCAN VEGA 3 LM, with Gatan
254 ChromaCL2UV at the SCMEM (GeoRessources, Nancy, France). *In situ* U-Pb and Lu-Hf
255 isotope analyses of zircon grains/domains were carried out by Laser Ablation Inductively
256 Coupled Plasma Mass Spectrometry (LA-ICPMS), at Goethe University Frankfurt am Main
257 (Germany). Laser spots for Lu-Hf isotope analyses (40 µm in diameter) were placed on top of

258 the U–Pb laser spots (33 μm in diameter) used for dating. The results of U-Pb dating and Lu-
259 Hf isotope analyses are shown in Tables 2 and 3 respectively. The values of zircon standards
260 are provided as supplementary material.

261

262 ***3.3. Re-Os dating of pyrite***

263

264 From selected drillcore intervals, centimetre-large pyrite grains (Py₄ proximal to auriferous
265 D_{4YA} veins) were separated using a saw and then crushed (GeoRessources, Nancy, France). Re-
266 Os analyses were performed on two aliquots of the crushed pyrite powder at the Centre de
267 Recherches Pétrographiques et Géologiques (CRPG) in Nancy, France. Chemical separation
268 techniques applied in this study are based on those described by Shirey and Walker (1995) for
269 sample digestion, using an Anton Paar HPA-S high pressure asher instead of Carius tubes, and
270 Birck et al. (1997) for osmium extraction. For each sample, ~ 200 mg of pyrite powder were
271 spiked with precisely weighed quantities of a mixed ¹⁸⁵Re-¹⁹⁰Os tracer solution and digested in
272 a mixture of hydrochloric acid (2 mL), nitric acid (5 mL) and hydrogen peroxide (0.1 mL) at
273 260 °C for 16 h, under a pressure of 100 bars. After sample digestion, Os was separated by
274 liquid–liquid extraction into liquid bromine. The Br₂ was then evaporated, and the osmium
275 fraction was purified by microdistillation (Birck et al. 1997). The Re was extracted from the
276 residual acidic solution by anion exchange using chromatographic columns (AG1 X8 resin). Re
277 isotopic compositions for isotope dilution calculations were measured using a Thermo Neptune
278 MC-ICPMS. Instrumental mass fractionation during measurements was regularly monitored
279 and corrected for using an 0.5 ppb Re standard with an assumed ¹⁸⁷Re/¹⁸⁵Re ratio of 1.6738.
280 The Os samples were loaded on platinum filaments for analysis by negative thermal ionization
281 mass spectrometry (N-TIMS; Creaser et al. 1991; Völkening et al. 1991), using a Finnigan
282 MAT 262 instrument. About 0.2 μL of a saturated solution of Ba(OH)₂ in 0.1 N NaOH (Birck
283 et al. 1997) was added to the samples to maximise OsO₃⁻ emission in the instrument. Analyses
284 were made by peak jumping and ion counting using an ETP electron multiplier. Instrumental
285 mass fractionation was corrected iteratively off-line by assuming that the true ¹⁹²Os/¹⁸⁸Os ratio
286 of the sample loaded on the filament lay on a mixing line between the spike (5.00736) and
287 natural (3.08271) values. The oxygen isotope composition determined by Nier (¹⁷O/¹⁶O =
288 0.0003708 and ¹⁸O/¹⁶O = 0.002045) was used to correct for isobaric interferences from heavy
289 oxides. Common Os, including both the natural component and any contribution from the
290 analytical blank, was monitored using mass ¹⁸⁸Os, and a correction to ¹⁸⁷Os was applied
291 assuming a common ¹⁸⁷Os/¹⁸⁸Os value of 0.6 ± 0.5 . The magnitude of this correction was about

292 0.02% for both aliquots. The Re blank associated with these samples was 24 ± 7 pg while the
293 total Os blank was 0.75 pg with a $^{187}\text{Os}/^{188}\text{Os}$ ratio of 6.1. The results of the Re-Os dating are
294 shown in Table 4. All uncertainties are 2σ , and include all identified sources of uncertainty,
295 including measurement uncertainties, blank variability, and the variation in the assumed initial
296 $^{187}\text{Os}/^{188}\text{Os}$ ratio of the pyrite.

297

298 ***3.4. Airborne geophysical data processing and interpretation***

299

300 Airborne geophysical data from (1) magnetic and (2) radiometric survey of Auplata Mining
301 Group are used for this study. The covered area, of 360 km^2 represents 2201 km of northwest-
302 southeast striking lines, using a line spacing of 200 m with perpendicular tie lines flown every
303 1000 m. The height above ground of the sensor is 100 m. Data include (1) airborne radiometric
304 data (K, Th, U) and (2) airborne magnetic data.

305 Airborne magnetic surveys help constraining structures and lithologies and are therefore
306 excellent tools for constructing lithostructural maps (Aitken & Betts, 2009a, b; Baratoux et al.,
307 2015) especially in undercover domains (Metelka et al., 2011). Raw data have been processed
308 using a variety of filters to enhance short and long wavelength features. The total magnetic field
309 data were reduced to the pole prior to further processing. Filters used include (1) the First
310 Vertical Derivative (1VD), (2) the Tilt Derivative (TD) and (3) the Horizontal Derivative
311 (Blakely & Simpson, 1986; Miller & Singh, 1994; Milligan & Gunn, 1997; Pilkington &
312 Keating, 2009; Verduzco et al., 2004). Regarding the radiometric data, the original bands K,
313 eTh, and eU and the ternary RGB (Red, Green, Blue) color composite are used. The gamma-
314 ray signal gives information regarding the content and distribution of the radioactive elements
315 in rocks. It can highlight anomalies due to geochemical alterations such as mineralization,
316 hydrothermal alterations, and weathering (Metelka et al., 2011). Finally, a SRTM digital
317 elevation model shaded from northwest is utilized as a background image.

318

319 **4. Geological results**

320

321 ***4.1. Petrography of quartz monzodiorite***

322

323 All magmatic rocks observed in drillcores are hydrothermally altered, and host abundant
324 auriferous veins formed during brittle deformation D_{4YA} (Combes et al., 2021a). Even the least
325 altered quartz monzodiorite samples provide evidence for albitization (Fig. 6A). Albite is
326 hydrothermal and associated with the syn- D_{4YA} brittle veining system. The rock is phaneritic,
327 fine to medium grained with no internal fabric. The observed mineral assemblage is albite,
328 quartz, sericite and chlorite, with minor amounts of ankerite, magnetite, calcite and apatite, even
329 though there are variation among the samples. Some samples show higher amounts of chlorite
330 and ankerite (Fig. 6B) and/or of hematite (Fig. 6C). Under the microscope, the predominant
331 minerals are quartz and albite, which commonly shows a polysynthetic twinning and evidence
332 for sericitization, and sericite (Fig. 7A and D). Minor K-feldspar was rarely observed in a few
333 samples (Fig. 7C). Some samples were affected by moderate to strong chloritisation (Fig. 7B).
334 Hydrothermal formation of ankerite (Fig. 7C and E) and/or hematite in interstitial domains
335 between albite grains is common (Fig. 7F), causing the typical reddish color of the rocks.

336

337 4.2. *Geochemistry of quartz monzodiorite*

338

339 Whole-rock geochemical data for the five least altered samples are provided in Table 1. SiO_2
340 contents range from 61.76 to 68.48 wt. % while Na_2O concentrations vary from 5.61 to 7.42
341 wt. %, and Fe_2O_3 contents range from 2.35 to 4.66 wt. %. As previously mentioned in Combes
342 et al. (2021a), these samples plot in the quartz monzodiorite field in the Q-A-P normative
343 classification diagram (Fig. 8A) and in the trondhjemite field (Fig. 8C), though this designation
344 must be taken with caution due to the great amount of hydrothermal albite. All five
345 representative samples plot in the same field in the relatively immobile elements Th vs Co
346 diagram (Fig. 8B), arguing for a single protolith for all the least altered samples. This protolith
347 belongs to the calc-alkaline series based on the AFM diagram of Irvine and Baragar (1971).

348

349 Regarding trace elements, the Y content is below 11 ppm for all samples. Chondrite-normalised
350 REE patterns (Sun and McDonough, 1989; Fig. 8D) are highly reproducible and show a high
351 degree of fractionation, characterized by a relatively steep slope from the LREE toward the
352 HREE. The data reveal: (1) LREE (La, Ce, Pr, Nd) enrichment with the La_N content ranging
353 from 90.81 to 109.23; (2) no marked Eu anomalies, and (3) $[La/Yb]_N$ ratios ranging from 20.7

354 to 38.6. The HREE patterns are shallowly dipping toward the right with low contents of HREE
355 (Er, Yb, Lu); the Yb_N contents range from 2.46 to 4.39.

356

357 A geochemical database of plutonic rocks sampled within French Guiana has been built for this
358 study (over 40 key analysed and dated samples). To constrain the geodynamical significance of
359 the quartz monzodiorite observed at Yaou and to integrate it into the context of known regional
360 plutonic events, the chondrite normalized REE (Sun and McDonough, 1989) pattern of this
361 rock is compared with patterns of the most representative samples of each main plutonic
362 complex in the region as illustrated in figure 9. Representative samples are from the "Ile de
363 Cayenne" Complex (Fig. 9A), the 1st generation of TTG-like patterns (Fig. 9B), the 2nd
364 generation of TTG-like (Fig. 9C), the late 2nd generation of TTG-like (Fig. 9D), the Granitic
365 suite (Fig. 9E) and the peraluminous leucogranite unit (Fig. 9F). Comparisons are discussed in
366 the *Discussion* section.

367

368 ***4.3. U-Pb dating and Hf isotope analyses***

369

370 Zircon grains from the quartz monzodiorite were dated *in-situ* by LA-ICP-MS (Table 2) and
371 analysed for Hf isotopes (Table 3). The dated zircon grains are euhedral to subhedral and vary
372 in length from 100 to 400 μm (Fig. 10A). BSE images reveal oscillatory or banded magmatic
373 zoning, even though many grains are more or less intensely altered and fractured (Fig. 10A).
374 All analyses, except one, show Th/U ratios >0.1 (Table 2) typical for magmatic zircon. Most
375 analyses yielded discordant U-Pb ages, which define a Discordia line with upper and lower
376 intercept ages at 2128.9 ± 5.1 Ma and 768 ± 210 Ma, respectively (Fig. 10B). The upper
377 intercept age is identical, within error, with a Concordia age of 2130.6 ± 5.8 Ma (MSWD =
378 0.15, Probability of concordance = 0.7) obtained by fifteen spot analyses (Figure 10C). The
379 Concordia age is interpreted to define the timing of magma crystallization, whereas the lower
380 intercept age points to Pb loss during a Neoproterozoic event. The analysed zircon grains show
381 a limited range in initial $^{176}\text{Hf}/^{177}\text{Hf}$ values between 0.281463 and 0.281588, corresponding to
382 suprachondritic εHf_t values between +1.3 and +4.2, and hafnium (two stage) model ages
383 between ca. 2.4 and 2.6 Ga (Fig. 10D, Table 3).

384

385

386

387 ***4.4. Re-Os dating of pyrite***

388

389 The quartz monzodiorite is a preferential host for the main gold-bearing vein set with a strong
390 rheological control (Combes et al. 2021a). These quartz-carbonate veins characterized by a
391 strong proximal pyritization postdate the intrusive event and are interpreted as being
392 synchronous to the D_{4YA} deformation phase. The Py₄ pyrite grains are coarse, homogeneous in
393 composition, and can contain gold micro-inclusions and gold infilling fractures. Two aliquots
394 of Py₄ from the same sample powder yield Re-Os ages of 2110±30 Ma and 2101±17 Ma (Table
395 4). The average age of 2105±25 Ma is considered, and is interpreted to date the timing of pyrite
396 precipitation cogenetic with Au mineralization during phase D_{4YA}.

397

398

399 **5. Geophysical interpretations**

400

401 ***5.1. Lithological distribution***

402

403 At the deposit-scale, the lithological distribution of the main units is relatively well identified
404 (Combes et al., 2021a) from drillcore data and historical subsurface extraction and mapping.
405 When zooming out from the central part of Yaou, no outcrop data are available at the district-
406 scale where no recent exploration work has been carried out within this dense Amazon Forest
407 area. Magnetic and radiometric anomalies are used here to zoom out and to produce a
408 lithological map up to the district-scale (i. e. beyond the Yaou tenement, see limits on Figure
409 3) with respect to the initial camp-scale map. All interpretations and corroborations between
410 geophysical data and available field/core observation are made first at the well-studied camp-
411 scale. The potassium anomaly map presented in Figure 11A defines in great details the spatial
412 distribution of the metasedimentary unit belonging to the Paramaca greenstone belt.
413 It corroborates the regional-scale map proposed by Delor et al. (2003b) based mainly on the
414 BRGM radiometric survey for the whole country (Fig. 2 and 3). At the camp-scale, this
415 correlation (positive K anomalies and metasediment distribution) is demonstrated where drilled
416 areas with logged metasediments show positive K anomalies. The U anomaly map delimits the
417 northeastern U-rich plutonic body (Fig. 11B) while a clear delimitation of both TTG-like
418 complexes (according to Delor et al., 2003b) is visible in the ternary map displaying the relative
419 abundances of U, K and Th (Fig. 11C). The Eastern body is defined by a clear blue-green
420 signature, in the gamma-ray spectrometry ternary image, associated with Fe-rich regolith

421 covers, this preferential deep weathering (residual or depositional regolith cover) allows to
422 precisely define this pluton.

423

424 The observations from the radiometric maps are supported by the 1VD grid (First Vertical
425 Derivative, Fig. 11D) emphasizing shallow features, with (1) the northeastern pluton delimited
426 by its smooth texture, (2) the eastern pluton highlighted by its smooth texture (but to a lesser
427 degree than the northeastern pluton), (3) the remanently magnetized dolerite dike striking
428 N165°, (4) the metasediments without stipple textures observed in the N as opposed to (5) the
429 main area with stipple textures typical of metavolcanite formations. Finally (6) some minor
430 mafic intrusive plugs are identified in the northern part of the surveyed area together with a
431 small circular late pluton (Fig. 11D). The whole interpreted lithological map is presented in
432 Figure 11E on a shaded-relief image. A strong uncertainty in lithology discrimination remains,
433 indeed the metasedimentary unit may be hidden by regolith as illustrated in Figure 11E with
434 identified areas of possible occurrences of residual or depositional regolith cover.

435

436 Overall, based on the internal geophysical data set of the Auplata Mining Group, the present
437 study proposes a more detailed lithological map compared to the one established by Delor et al.
438 (2003b) for the whole country using the BRGM regional data set. The occurrence of the
439 metasedimentary unit is extended toward the south and the TTG-like complexes are better
440 delimited at their western borders. Unfortunately, the quartz monzodiorite bodies, which are
441 well defined at the camp-scale could not be targeted with the resolution of the present data set.

442

443 ***5.2. Identified structures***

444

445 No robust structural data are available for the area. Three filters are therefore used in an attempt
446 to identify possible structures within the Yaou district, namely the 1VD (Fig. 12C), RTP-TD
447 (Fig. 12A), and RTP-TD-HDR (Fig. 12 B) filters (see *methods* section). This work focuses here
448 on the supra-crustal-scale only. As for the lithologic distribution, the study focuses first on the
449 deposit to camp-scale and then zooms out. From core studies and internal reports, the identified
450 structures at the camp-scale are as follow: a main subvertical foliation striking east-west and a
451 shear corridor striking N60° (corresponding to the CYSZ, Combes et al., 2021a). While it is not

452 possible with the used magnetic data set to define at this scale the main foliation, the CYSZ
453 may correspond to a low magnetic N60°-striking lineament. Considering all filters, at the camp-
454 scale, structures observed are low and high magnetic response northeast-southwest-striking
455 linear structures. Locally, they may be offset by a N140° structure. When zooming out and
456 considering the whole surveyed area (Fig. 3 and 12), possible interpreted structures can be
457 defined as follow:

458

459 (1) The main lineaments strike roughly northeast-southwest (Fig. 12A, B), the RTP-TD
460 (Tild Derivative) filter enhancing these magnetic lineaments that may correspond to a
461 series of sub-parallel vertical features that could reflect a dipping stratigraphy or
462 deformation fabric. These main structures are truncated by the dolerite and in the E, are
463 parallel to contacts between the metavolcanites and the TTG-like complexes and seem
464 wrapped around these complexes in the magnetic data. They locally display some
465 folding together with some minor sinistral strike-slip faulting offsetting the main
466 lineaments (northeast of the area, Fig. 12D);

467

468 (2) Some minor fabrics within the metasedimentary unit, in the northwest part of the area,
469 show a weak magnetic intensity signal (Fig. 12C). In this area the main northeast-
470 trending lineaments are not observed;

471

472 (3) Within the TTG-like complexes in the E, some internal northeast-southwest features are
473 highlighted by the RTP-TD-HDR filter (Fig. 12B), suggesting that the TTG-like
474 complexes have been affected by the deformation phase giving the main north northeast-
475 south southwest lineaments and were emplaced before the main deformation phase.
476 Margins of these plutons show a negative magnetic anomaly (Fig. 12C);

477

478 (4) The same minor N140° faults observed at the camp-scale are encountered elsewhere in
479 the surveyed area (in red in Figure 12D) affecting the main northeast-southwest
480 structures. Most gold occurrences (established by the BRGM, Guyanor and Auplata
481 Mining Group-internal reports) are located in the vicinity of interconnections between
482 these minor faults and the main lineaments (see Fig. 12D for some examples, other
483 occurrences are not included here for confidentiality issues);

484

485 (5) Two parallel features, striking around 10 degrees east of north are truncating the
486 northeast-southwest main lineaments (Fig. 12 C). Their extension toward the south
487 could not be traced with the used geophysical data set.

488

489 The scale of the geophysical maps is not sufficiently detailed to delimitate the CYSZ which
490 may also be hidden by high and low magnetic lineaments. The N60° low magnetic lineaments
491 are continuous along strike and replicated toward the northwest (Fig. 12-A, B, C and D) and
492 may correspond to potential shear zones.

493

494

495

496

497 **6. Discussion**

498

499 ***6.1. The Yaou intrusive event at the deposit-scale***

500

501 ***6.1.1. Geochemical signature***

502

503 Plots of trace elements normalized to primitive mantle abundances (Sun and McDonough, 1989,
504 Fig. 8E), show patterns enriched in highly incompatible trace elements (LREE), depleted in
505 HREE and enriched in large-ion lithophile elements (LILE) such as Rb, Ba, U and Pb. We
506 observe a depletion in Cs, an enrichment in Sb and negative anomalies in Nb-Ta-Ti (Fig. 8E).
507 The Nb/Ta ratios are subchondritic ($\text{Nb/Ta} \leq 12.57$ ppm).

508

509 These REE data from the Yaou quartz monzodiorite are compared to REE results from other
510 plutonic rocks sampled within French Guiana in Fig. 9. The « Ile de Cayenne » complex
511 samples show a flat pattern with no variation between LREE and HREE together with an Eu
512 negative anomaly (Fig. 9A) that differs strikingly from the quartz monzodiorite's pattern. The
513 Yaou samples share some similarities with the 1st generation of TTG-like but those TTG display
514 more depleted HREE and a marked positive Eu anomaly (Fig. 9B). The Yaou quartz
515 monzodiorite pattern clearly resembles those of the 2nd generation of TTG-like (Fig. 9C), with
516 an enrichment in LREE and a depletion of HREE. It is even better correlated with the pattern
517 of the late samples of the same TTG-like generation, as visible in Figure 9D. Therefore,

518 geochemically, the Yaou quartz monzodiorite can be interpreted as belonging to the 2nd TTG-
519 like generation, also referred to as the Central TTG-like Complex (Delor et al., 2003a, b) and
520 dated between ca. 2140-2120 Ma for the main magmatic phase and ca. 2113-2101 Ma (Enjolvy,
521 2008; Fig. 9) for the late phase interpreted as a continuum of the same 2nd generation TTG-like
522 magmatic event. Samples of the granitic suite follow a similar pattern to those of Yaou (Fig.
523 9E) but with much stronger REE absolute abundances and no relative Ho enrichment. Finally,
524 peraluminous leucogranite samples show higher absolute LREE abundances, strong negative
525 Ce and Eu anomalies, and a slightly sloping HREE segment, with absolute HREE abundances
526 greatly exceeding those of the Yaou samples.

527

528 The interpretation of a TTG-type intrusion at Yaou is reinforced by the similarities between the
529 Yaou samples and the typical TTG geochemical signatures (Martin et al., 2005; Moyen and
530 Martin, 2012). Indeed, Moyen and Martin (2012) indicates that TTGs (1) do not present Eu
531 anomalies, as for the Yaou samples, (2) show Yb content below 1.5 ppm (below 0.8 ppm for
532 our samples), (3) an $(La/Yb)_N > 15$ where the normalized ratios at Yaou are above 20.65 ; (4) a
533 depletion in HREE and Y (same depletion for Yaou and a Y content below 11 ppm) and (5)
534 Nb-Ta negative anomalies, also observed for this study with $Nb/Ta < 13$ ppm. TTG magmas
535 result from melting and/or crystallization of hydrous low-potassium basalts (Moyen and Martin,
536 2012). The geodynamic setting in which they are formed is still debated (Laurent et al., 2020).
537 The low content of HREE implies the presence of garnet in the petrogenesis of the magma,
538 either as residual or fractionating phase. Considering its stability field, it is therefore at high-
539 pressure conditions (>1.2 GPa, *i.e.* at >40 km depth). The Yaou quartz monzodiorite could have
540 formed in an active margin context (i) by partial melting of a subducted oceanic crust, (ii) by
541 melting of over-thickened arc roots or (iii) by fractionation of hydrous arc basalts (Laurent et
542 al., 2020 and references therein).

543

544 ***6.1.2. Timing of magmatism and gold mineralization***

545 The Yaou gold deposit, mainly hosted by the quartz monzodiorite dated at ca. 2130 Ma, is
546 located in the vicinity of the Central TTG-like Complex with two complexes in the east (Fig.
547 2) belonging to the 2nd generation of TTG-like described by Delor et al. (2003a, b) and dated
548 between ca. 2140-2120 Ma. Therefore, the quartz monzodiorite intrusions identified at the
549 camp-scale could be associated (genetically and spatially) with these TTG-like complexes; yet

550 outcrops of these two eastern intrusions are currently unknown for further geochemical studies.
551 An interpreted integration of the deposit/camp-scale litho-structural framework in the regional-
552 scale scheme of Delor et al. (2003a, b) is presented in Figure 13 based on the robust timing of
553 emplacement of the pre- to syn-shearing intrusion together with the geochemical comparison
554 (REE patterns) of all types of magmatic rocks from French Guiana. Regarding the Re-Os pyrite
555 age, the duplicate analyses are in excellent agreement and yield an average value of 2105 ± 25
556 Ma. It suggests that the D_{4YA} phase was concomitant with the regional D_{2a} episode of Delor et
557 al. (2003a, b) and most likely postdated the intrusive event dated at 2130.6 ± 5.8 Ma. This is in
558 agreement with the relative timing of Combes et al. (2021a) based on core observations. It is
559 the first dating of a gold-bearing mineral in the region, allowing to bracket an absolute age of a
560 major gold event. Considering the obtained U-Pb and Re-Os ages for the intrusive event and
561 the D_{4YA} phase respectively, the following interpretation can be proposed: (1) the D_{1YA}/D_{2YA}
562 deformation phase would refer to the regional D_1 deformation phase (subduction, oceanic island
563 arcs/back arc basins dated between ca. 2180-2130 Ma with an N-S compression); (2) the $D_{3/4YA}$
564 would be related to the D_{2a} phase (collision, compression to transpression dated between ca.
565 2110-2080 Ma). The major gold event is interpreted here to occur between ca. 2130-2125 Ma
566 (latest age of the intrusion; the Au-bearing pyritization being post-crystallization) and ca. 2084
567 Ma (youngest age obtained on Py_4 permitted within uncertainties). The present work shows an
568 age of intrusion emplacement at the transition between the regional D_1 and D_{2a} , therefore at the
569 end of the magmatic arc activity (ca. 2180-2130 Ma) and at the beginning of the collision
570 between magmatic arcs and crustal blocks (ca. 2110-2080 Ma). We propose that the $D_{1/2YA}$
571 deformation phase ends earlier than initially proposed by Delor et al. (2003bs) for the D_1 phase
572 (ca. 2180-2130 Ma) as the Yaou intrusion (ca. 2130 Ma) is interpreted as post- D_{2YA} (Combes
573 et al., 2021a). Also, the D_{2a} deformation phase (dated at ca. 2110-2080 Ma), which is interpreted
574 to correspond to the D_{3YA} phase at Yaou, could start earlier. The D_{2a} has only been dated in the
575 northern belt of the PGB and not in the southern belt where the Yaou deposit is located (see
576 Fig. 13). Regarding the late Granitic suite (ca. 2110-2070 Ma, Pb/Pb and U-Pb on zircon dating,
577 see Fig. 13), both their geochemical signature (Fig. 9) and the relative timing of deformation
578 phases (Fig. 13) distinguish these rocks from the intrusive rocks of Yaou.

579

580 Regarding the isotopic data, zircon Hf isotope compositions are supra-chondritic suggesting
581 that the quartz monzodiorite derives from the reworking of Neoproterozoic-Siderian juvenile
582 components as old as ca. 2.6-2.4 Ga. The juvenile character of the Yaou intrusion reinforces

583 the interpretation of a TTG-like signature of the quartz monzodiorite. These Hf-isotopes
584 signatures are similar to those calculated on the intrusive rocks studied by Parra-Avila et al.
585 (2018, 2019) in the Baoulé-Mossi domain of the southern West African Craton with
586 $^{176}\text{Hf}/^{177}\text{Hf}_{(t)}$ values, ranging from 0.2814 to 0.2815 (Parra-Avila et al., 2018, 2019), witnessing
587 that their magma source area is quite similar.

588

589 ***6.2. Zooming out from the camp-scale, a pre- to syn-shearing intrusive event***

590

591 ***6.2.1. 2D considerations***

592

593 The spatial distribution of the intrusive bodies (aligned along a N60° trend) and their 3D
594 geometry has been defined in great details at the deposit to camp-scale (Fig. 4 and 5). The use
595 of geophysics where no ground exploration has been carried out is therefore essential although
596 the resulting interpretation may be weak. The CYSZ precisely delimited at the camp-scale and
597 striking N60° corresponds to a low magnetic lineament (Fig. 14A, B). A lateral repetition of
598 N60° structures toward the northwest (Fig. 14A) with alternating first order high and low
599 magnetic structures are interpreted. The high magnetic response may correspond either to (1) a
600 dipping stratigraphy possibly wrapped around the regional-scale plutons, or (2) fold hinges with
601 horizontal axial traces (Metelka et al., 2011; Baratoux et al., 2015).

602 An interpretation is here proposed (Fig. 14 B) with the possible occurrence of a series of parallel
603 shear zones located in low magnetic response areas (see the inferred D_{3YA} shear zones in Fig.
604 14B). These parallel shear zones may (1) be related to a regional tectonic stress field (poorly
605 constraint in the southern PGB; Delor et al., 2003b) or (2) be due to localization around a pair
606 of large plutons (the plutons being emplaced prior to at least some of the deformation).

607

608 Regarding the quartz monzodiorite intrusion, the resolution of the geophysical maps does not
609 allow to precisely delineate the intrusive bodies but possible occurrences using a correlation (as
610 observed within Yaou Central) between demagnetized lineaments and altered intrusions is
611 proposed (Fig. 14C). This association could be explained by the fact that quartz monzodiorite
612 bodies display a high frequency of D_{4YA} veins (Combes et al., 2021a) which produce magnetite-
613 depleted (and pyrite-rich) zones due to the progressive replacement of magnetite by pyrite
614 towards the veins by sulfidation reactions.

615

616 Importantly, brittle faults (west northwest-east southeast) are interpreted as being D_{4YA} -related
617 since these faults affect the interpreted D_{3YA} structures. Furthermore, these faults are all located
618 within known auriferous zones (near placers and/or gold showings such as Chaina, Tomantoni
619 and the Yaou Central area, Fig. 3) and share similar strikes with the regional $N120-140^\circ$
620 structures. However, the largest offset identified is associated with an east-west fault (Fig. 12
621 B, C, D) and does not correspond to any known gold showing.

622

623 *6.2.2. 3D considerations*

624

625 From these 2D interpretations, a 3D model can be discussed that integrates time as a component.
626 We interpret the relative timing of the shearing event and intrusive event at the camp-scale as
627 follow. First, the Pre- D_{3YA} phase D_{2YA} (Combes et al. 2021a), is characterized by an east-west
628 penetrative foliation (Fig. 15A) with both the metasediments and the metavolcanites being
629 transposed in the S_2 . The following syn- D_{3YA} shearing phase with the intrusive body is
630 illustrated in Figure 15B. A 3D representation of the interpreted shearing-induced intrusive
631 event is presented in Figure 15C with opening from shearing, associated magma injection
632 emplacement and lateral repetition of syn-kinematic intrusions and shear zones. Two
633 hypotheses are presented (Fig. 15C) that may explain the space opening in order to allow the
634 intrusions between the parallel shear zones. Robust structural data would be needed to test these
635 models. The first model implies the formation of tension gashes, which will rotate and deflect
636 while the shearing is active. The second model implies a syn-shearing back-rotation of fabrics
637 between the two shear zones, with an antithetic rotation. In this case the extension allowing
638 magma injection is unsure. A structural overview at the plan view of the spatial relationship
639 between the C/S_3 fabrics (associated with the D_{3YA} deformation phase) and the S_2 fabrics
640 (associated with the D_{2YA} deformation phase) is proposed in Figure 15D. This relationship may
641 reflect a protracted process during which intrusion emplacement and shearing are
642 synchronous.

643

644 Shear zone kinematic evidence (transtensional versus transpressional regime) is rare due to the
645 lack of bedrock outcrops. Thus, it is contentious to ascertain the role of shearing. Since the

646 CYSZ is parallel to the TTG-like complexes in the E, one simple interpretation could be that
647 the shearing expressed at Yaou would be related to emplacement of these TTG-like complexes.
648 Alternatively, the plutons may have already been emplaced and deformation has been localized
649 at their margins.

650

651 Yet, a more detailed structural study is needed to confirm the genetic link between shearing and
652 magmatism at smaller scale. Based on the geometry of the deposit at the camp-scale and the
653 geophysical interpretation at a smaller scale, we propose that the shearing could open spaces
654 (extensional pull-apart-like structures; Bhattacharya & Kar, 2004) enabling the magma to rise
655 and allowing the emplacement of various intrusive bodies along the shear structure (D'Lemos
656 et al., 1992; Weinberg et al., 2004). Weinberg et al. (2004) suggest « *that magma ascent in
657 shear zones is intermittent and characterized by magma entrapment, ballooning, renewed
658 escape, and deflation as the system develops into a number of dilational sites in shear-zone
659 shoulders interconnected by magma sheets within the shear zones* ». The process of magma
660 injection into a transtensional shear zone is exemplified within the Variscan belt, southwest Iberia
661 by Pereira et al. (2015). Similar settings are described by Hutton (1982), Guineberteau et al.
662 (1987); Joly et al. (2007) and Gébelin et al. (2007) but have been debated by Paterson and
663 Fowler (1993), Paterson and Schmidt (1999) and Paterson et al. (2005) regarding the role/need
664 of shear zones to provide a setting for the intrusions. An alternative model proposed by Neves
665 et al. (1996) is a pluton-assisted shear zone nucleation (referred as pluton-induced shear zone).
666 Here shear zones are related to magma emplacement as mentioned for the Borborema Province
667 of northeast Brazil with examples of intrusive bodies inducing strain localization and favoring
668 shear zone nucleation (Neves et al., 1996; Neves et al., 2005). More recently, Dering et al.
669 (2019) defined intrusion-related deformation as lateral/vertical propagation and inflation of
670 dikes that generates both seismicity and deformation (Dering et al., 2019 and references
671 therein).

672

673 Regarding the type of lithosphere involved in such compressive regime, two models are
674 currently considered, namely (1) the horizontal tectonic model, followed by Vanderhaeghe et
675 al. (1998) and Delor et al. (2003b) in the region, implying a modern-type tectonic where the
676 lithosphere is defined as resistant and cold; and (2) the vertical tectonic model as defined by
677 Gapais (2018) following the work of Cagnard et al. (2006a), Chardon et al. (2009) among other,
678 with a weak and hot/buoyant lithosphere. The proposed model at the Yaou camp-scale does not

679 allow us to decipher between a cold vs. hot orogenic setting without more structural data and
680 absolute dating of the related fabric.

681

682

683 *6.3. From the camp- to the district-scale, a new litho-structural model for gold targeting*

684

685 A new litho-structural map is constructed at the district-scale (Fig. 16A) based on deposit-scale
686 geological data (Combes et al., 2021a), 3D orebodies modelling, geochemical characterization
687 of intrusions and airborne geophysical interpretations. When compared to the cross-section of
688 Delor et al. (2003b) for the Yaou district as presented in Figure 16B the proposed lithologic
689 distribution is similar although the present study better defines the structural grain, the brittle
690 faults (D_{4YA}-related) and internal fabrics within the pre-deformation intrusive complexes.
691 Importantly, the two plutons now appear separated by a metavolcanite unit of the Paramaca
692 Greenstone Belt (Fig. 16 C).

693

694 This integrated approach, and in particular the interpretation of airborne geophysical data, led
695 to important findings and targeting keys previously unrecognized in the southern PGB. Indeed,
696 best targets include (1) intersections of the main northeast-southwest lineaments with late
697 N140° faults (many known occurrences follow this scheme); (2) near contacts of TTG-type
698 intrusions and (3) areas in the northwest where occurrences in metasediments are inferred. As
699 suggested by Combes et al. (2021a), the metasedimentary unit could be a primary source of
700 gold (Au-bearing Py₀).

701

702 Obtaining and interpreting geochronological, geochemical and geophysical datasets while
703 downscaling progressively from the ore shoot-scale to the metallogenic province is critical in
704 the mineral system approach. Within the southern PGB (where the Yaou deposit is located), the
705 following key parameters have to be considered to target new deposits, namely a favorable
706 architecture (whole-lithosphere plumbing system), a geochemical fertility (sources of ore
707 metals) and a favorable geodynamic framework (key geological settings with transient events);
708 (McCuaig and Hronsky, 2014; Wyman et al., 2016; Hronsky, 2019; Niiranen et al., 2019;
709 Groves et al., 2020 and references therein). In that sense, the three following aspects must be
710 examined:

711

712 (1) At all stages of exploration, a detailed petro-structural framework, at the deposit-scale,
713 needs to be built (e.g., Thébaud et al., 2018; Tedeschi et al., 2018a, b; Perret et al., 2020;
714 Combes et al., 2021a) with relative and absolute constraints of deformation phases,
715 veining system and lithologies (depending on available rocks and suitable minerals for
716 dating). The dating of the possible shearing and/or intrusive events are required to
717 understand the gold system of intrusion-hosted gold deposits spatially associated with
718 shear zones. A time window for gold deposition is evidenced in this study (ca. 2130-
719 2080 Ma; Fig. 13) which would be post- intrusive event (ca. 2130 Ma), and syn- to post-
720 shearing. This work confirms the conclusions of Milesi et al. (2003) considering that
721 the main gold event is located between the late crustal growth phase (late regional D₁)
722 and the crustal reworking phase (regional D_{2a}). Geochronology can then be used as an
723 exploration tool in the southern PGB.

724

725 (2) Concerning the potential hosting units, this study highlights the importance of 2 m to
726 80 m wide quartz monzodiorite bodies (TTG-like) in building a gold deposit where
727 orebodies volumes are depending on intrusions 3D geometries. The precise delimitation
728 of lithological units/facies with similar rheological and geochemical characteristics
729 representing traps for ore shoots is essential in the southern PGB with detailed
730 geochemical characterization and comparison/correlation of geochemical signatures at
731 various scales. Along this, the metasedimentary unit (of the PGB), that hosts gold-
732 bearing diagenetic pyrite grains (Combes et al., 2021a) can be mapped using K
733 anomalies radiometric datasets (Fig. 11A). The north western part of the Yaou district
734 is highly promising in that sense with the presence of large metasedimentary domains,
735 locally covered by a deep weathering profile (Fig. 11E and 16A). Overall, as stated by
736 Cassard et al. (2008), the gold trends (observed or inferred) are localized preferentially
737 in the metavolcanites and metasediments of the PGB or at contacts between these
738 sequences and the TTG-like complexes (Milesi et al., 2003; Delor et al., 2003b). These
739 rocks (metavolcanites and metasediments) thus present potential sources for orogenic
740 gold (Phillips and Groves, 1983; Groves et al. 1998; Pitcairn et al., 2006; Large et al.,
741 2009; Phillips and Powell, 2010).

742

743 (3) Regarding the favorable architecture, the ore shoot distribution, at the deposit-scale,
744 depends notably on micro deformation, with gold (re-) mobilization, liberation and re-
745 precipitation (Fougerouse et al., 2016 and references therein). This control has been
746 discussed at Yaou (Combes et al., 2021a) with a polyphase deformation and
747 hydrothermal activity. Having no field-based structural data when zooming-out at the
748 district to the camp-scale, transcurrent shear corridors interpreted from the airborne
749 magnetic surveys must be defined and tested. Related to the eburnean-transamazonian
750 orogenic system (Delor et al., 2003b; Chardon et al., 2020), these structures are of
751 primary importance. The gold mineralization at Yaou being hosted by intrusive bodies
752 and the N60°-striking shear corridor, these two gold-bearing features need to be
753 recognized by both geological and airborne/ground geophysical surveys but also by
754 drilling (oriented drill core) with precise 3D modelling of the geometry of the deposit
755 (as previously proposed by Allibone et al., 2018; Cowan et al., 2019; Kreuzer et al.,
756 2019 for example)

757

758 Within the southern PGB, large-scale structures as paleo-convergent margins need to be
759 targeted and outlined by airborne geophysical methods. It is worth noticing that Yaou is located
760 near the lithospheric-scale shear zones inherited from the transamazonian orogeny referred as
761 the CGSZ, (Central Guiana Shear Zone; Lasserre et al., 1989) which is a highly promising
762 lineament that may ensure the circulation of gold-bearing fluids through the crust (McCuaig
763 and Hronsky, 2014, Groves et al., 2020b). The prospecting potential of the area is high, with
764 possible features associated with mineralization, such as faults and intrusions, that can be
765 mapped at the district-scale (recognized by both geological and airborne/ground geophysical
766 data), (e.g., Stewart et al., 2009; Metelka et al., 2011; Baratoux et al., 2015). There, a particular
767 focus has to be made on lineaments parallel to lithological contact between the TTG-like
768 complexes and the volcanosedimentary packages (similar to the CYSZ).

769

770 At the cratonic-scale, gold deposits spatially associated with intrusions bodies within the Guiana
771 Shield include the Omai gold deposit (Guyana, Voicu et al. 1999; 2001), which displays intrusive
772 rocks dated at ca. 2107-2081 Ma (U-Pb on zircon; Norcross et al. 2000). The so-called Omai
773 Stock (quartz monzodiorite) of Voicu et al. (1999) displays a REE chondrite-normalized pattern
774 similar to that of the Yaou intrusion but with a slight enrichment in HREE. Like the Yaou quartz

775 monzodiorite, the Omai intrusion postdates the regional foliation and is affected by a late phase
776 of brittle deformation responsible for the network of Au-bearing veins (Voicu et al., 1999;
777 2001). The targeting of quartz monzodiorite intrusive bodies with TTG-like signatures, in the
778 vicinity of shear zones, should be considered in the whole region. The intrusion-hosted Yaou-
779 type deposit may not be unique, similar structural settings may be considered as exploration
780 targets in the Yaou and Dorlin districts.

781

782 **7. Conclusions**

783

784 The Yaou intrusion hosting the bulk of the gold mineralization, is dated at 2130.6 ± 5.8 Ma (U-
785 Pb on zircon) and show supra-chondritic ϵ_{Hf_t} indicating that this quartz monzodiorite is derived
786 from the reworking of Neoproterozoic-Siderian juvenile components. Using geochemical
787 comparison (REE patterns) of all types of plutonic rocks from French Guiana, the quartz
788 monzodiorite is associated to the 2nd stage TTG-like rocks, which have the same age range. An
789 integration of the deposit-scale framework is proposed where the quartz monzodiorite
790 emplacement is defined between the regional D₁ and D_{2a} phases, therefore at the end of the
791 crustal growth phase and at the beginning of the crustal reworking period. The main gold event
792 hosted by this intrusion is dated by Re-Os on Au-bearing pyrite at 2105 ± 25 Ma. In an outcrop-
793 depleted region with no robust structural data, the multi-scale approach using airborne magnetic
794 and radiometric data, helps to better understand the spatial distribution of the intrusions and
795 associated shear zones. Both are interpreted as being repeated along a N60° trends and laterally
796 toward the northwest. The coupled geological and geophysical studies used in French Guiana
797 are promising to localise/predict which structures and lithologies could be associated with gold
798 at the district-scale. The Yaou-type intrusion-hosted mineralization may be targeted along the
799 N60° structures and where possible occurrences of intrusive bodies are defined. Moreover,
800 minor faults offsetting the D_{3YA} N60° structures are high priority targets, knowing that the main
801 gold event at Yaou is associated with the D_{4YA} deformation phase. This integrated approach,
802 and in particular interpretation of airborne geophysical data, opens some targeting possibilities,
803 previously unrecognized within the southern Paramaca Greenstone Belt (PGB) at the province-
804 scale.

805

806 **Acknowledgment**

807

808 This study is part of Vincent Combes's Ph.D. research at the Université de Lorraine within the
809 GeoRessources laboratory, in Nancy, France. We are grateful to E. Davy of the CRPG in Nancy,
810 France for helping us with zircon separation, to J. Perret for zircon handpicking and to D.
811 Chardon, A. Chauvet and T. Torvela for the scientific discussions on this study. The airborne
812 geophysical data were reprocessed and interpreted during the SAXI workshop held in 2019 at
813 Paramaribo, Suriname. Two anonymous reviewers are acknowledged for their careful reviews
814 which have improved this manuscript substantially. V. Oliveros is thanked for the editorial
815 work.

816

817 **Funding**

818 This research was funded by Auplata Mining Group (AMG) and benefited from the framework
819 of the CREGU.

820

821 **References**

822

823 Aitken, A.R.A., Betts, P.G., 2009a. Constraints on the Proterozoic supercontinent cycle from
824 the structural evolution of the south-central Musgrave Province, central Australia.
825 *Precamb. Res.* 168, 284–300.

826 Aitken, A.R.A., Betts, P.G., 2009b. Multi-scale integrated structural and aeromagnetic analysis
827 to guide tectonic models: an example from the eastern Musgrave Province, Central
828 Australia. *Tectonophysics* 476, 418–435.

829 Allibone, A., Blakemore, H., Gane, J., Moore, J., Mackenzie, D., Craw, D., 2018. Contrasting
830 Structural Styles of Orogenic Gold Deposits, Reefton Goldfield, New Zealand. *Econ. Geol.*
831 113 (7), 1479–1497.

832 Barker, F., 1979, Trondhjemite: Definition, environment, and hypotheses of origin: p. 1-12, in
833 Barker, F., ed., *Trondhjemites, Dacites, and Related Rocks*, Elsevier, Amsterdam, 659 p.

834 Baratoux, L., Metelka, V., Siebenaller, L., Naba, S., Naré, A., Ouyia, P., Jessell, M.W., Béziat,
835 D., Salvi, S., and Franceschi, G., 2015. Tectonic evolution of the Gaoua region:
836 Implications for mineralization. *J. Afr. Earth Sci.* 112, 419–439.

837 Begg, G.C., Hronsky, J.A.M., Arndt, N.T., Griffin, W.L., O'Reilly, S.Y., Hayward, N., 2010.
838 Lithospheric, cratonic, and geodynamic setting of Ni–Cu–PGE sulfide deposits. *Econ.*
839 *Geol.* 105, 1057–1070.

840 Betts, P. G., Williams, H. A., Stewart, J. R., Ailleres, L., 2007. Kinematic analysis of
841 aeromagnetic data: looking at geophysical data in a structural context. *Gondwana Res.*
842 11(4), 582 - 583.

843 Bhattacharya, S., Kar, R., 2004. Alkaline intrusion in a granulite ensemble in the eastern ghats
844 belt, India: Shear zone pathway and a pull-apart structure. *J Earth Syst Sci.* 113, 37–48
845 <https://doi.org/10.1007/BF02701997>

846 Bierlein, F.P., Groves, D.I., Goldfarb, R.J., Dubé, B., 2006. Lithospheric controls on the
847 formation of provinces hosting giant orogenic gold deposits. *Miner. Depos.* 40, 874–887.

848 Bierlein, F.P., Groves, D.I., Cawood, P.A., 2009. Metallogeny of accretionary orogens—the
849 connection between lithospheric processes and endowment. *Ore Geol. Rev.* 36, 282–292.

850 Birck, J.-L., Roy Barman, M., Capmas, F., 1997. Re-Os isotopic measurements at the
851 femtomole level in natural samples. *Geostand. Newsletter* 20, 19–27.

852 Blakely, R.J., Simpson, R.W., 1986. Approximating edges of source bodies from magnetic or
853 gravity anomalies. *Geophysics* 51, 1494–1498.

854 Blichert-Toft, J., Puchtel, I.S., 2010. Depleted mantle sources through time: Evidence from Lu-
855 Hf and Sm-Nd isotope systematics of Archean komatiites. *Earth Planet. Sci. Lett.* 297,
856 598–606.

857 Bouvier, A., Vervoort, J.D., Patchett, P.J., 2008. The Lu–Hf and Sm–Nd isotopic composition
858 of CHUR: Constraints from unequilibrated chondrites and implications for the bulk
859 composition of terrestrial planets. *Earth Planet. Sci. Lett.* 273, 48–57.

860 Cagnard, F., Durrieu, N., Gapais, D., Brun, J.P., Ehlers, C., 2006a. Convergence tectonics
861 within weak lithospheres : a working hypothesis with particular reference to Precambrian
862 times. *Terra Nova* 18: 72–78.

863 Carignan, J., Hild, P., Mevelle, G., Morel, J., Yeghicheyan, D., 2001. Routine Analyses of Trace
864 Elements in Geological Samples using Flow Injection and Low Pressure On-Line Liquid
865 Chromatography Coupled to ICP-MS: A Study of Geochemical Reference Materials BR,
866 DR-N, UB-N, AN-G and GH. *Geostandards and Geoanalytical Research* 25, 187–198.
867 <https://doi.org/10.1111/j.1751-908X.2001.tb00595.x>

868 Cassard, D., Billa, M., Lambert, A., Picot, J., Husson, Y., Lasserre, J., Delor, C., 2008. Gold
869 predictivity mapping in French Guiana using an expert-guided data-driven approach based
870 on a regional-scale GIS. *Ore Geol. Rev.* 34. 471-500.

871 Creaser, R.A., Papanastassiou, D.A., Wasserburg, G.J., 1991. Negative thermal ion mass
872 spectrometry of osmium, rhenium and iridium. *Geochim. Cosmochim. Acta* 55, 397–401.

873 Chardon, D., Gapais, D., Cagnard, F., 2009. Flow of ultra-hot orogens: a view from the
874 Precambrian, clues for the Phanerozoic. *Tectonophysics* 477: 105–118.

875 Chardon, D., Bamba, O., Traoré, K., Eburnean deformation pattern of Burkina Faso and the
876 tectonic significance of shear zones in the West African craton, 2020. *BSGF-Earth Sci*
877 *Bull.* 191, 2.

878 Combes, V., Eglinger, A., André-Mayer, A.-S., Teitler, Y., Heuret, A., Gibert, P., Béziat, D.,
879 2021a. Polyphase gold mineralization at the Yaou deposit, French Guiana. In: Torvela, T.,
880 Chapman, R.J., Lambert-Smith, J. (Eds.), Geological Society, London, Special
881 Publications. 516, <https://doi.org/10.1144/SP516-2020-29>

882 Cowan, E.J., 2020. Deposit-scale structural architecture of the Sigma-Lamaque gold deposit,
883 Canada—insights from a newly proposed 3D method for assessing structural controls from
884 drill hole data. *Miner Deposita* 55, 217–240. <https://doi.org/10.1007/s00126-019-00949-6>

885 Delor, C., Lahondère, D., Egal, E., Lafon, J.-M., Cocherie, A., Guerrot, C., Rossi, P., Truffert,
886 C., Théveniaut, H., Phillips, D., Avelar, V.G.d., 2003b. 2-3-4 In: Transamazonian crustal
887 growth and reworking as revealed by the 1:500000 scale geological map of French Guiana.
888 *Géol Fr.* 5–57.

889 Delor, C., de Roever, E.W.F., Lafon, J.-M., Lahondère, D., Rossi, P., Cocherie, A., Guerrot, C.,
890 Potrel, A., 2003a. The Bakhuis ultrahigh-temperature granulite belt (Suriname) : II.
891 Implications for late Transamazonian crustal stretching in a revised. *Géol Fr.* 2-3- 4, 207–
892 230.

893 Dering, G. M., Micklethwaite, S., Cruden, A. R., Barnes, S. J., Fiorentini, M. L.,
894 2019. Evidence for dyke parallel shear during syn-intrusion fracturing. *Earth Planet. Sci.*
895 *Lett.* 507, 119–130. <https://doi.org/10.1016/j.epsl.2018.10.024>

896 De Roever, E.W.F., Lafon, J.-M., Delor, C., Cocherie, A., Rossi, P., Guerrot, C., Potrel, A.,
897 2003. The Bakhuis ultrahigh-temperature granulite belt (Suriname): I. petrological and
898 geochronological evidence for a counterclockwise P-T path at 2.07–2.05 Ga. *Géol. Fr.* 2-
899 3-4, 175–205.

900 D'Lemos, R. S., Brown, M. and Strachan, R. A., 1992. Granite magma generation, ascent and
901 emplacement within a transpressional orogen. *J. Geol. Soc. of London.* 149, 487-490.

902 Egal, E., Mercier, D., Itard, Y., Mounié, F., 1992. L'ouverture de bassins en pull-apart au
903 Protérozoïque inférieur: nouveaux arguments dans le nord du craton guyanais. *Comptes*
904 *rendus de l'Académie des sciences. Série 2, Mécanique, Physique, Chimie, Sciences de*
905 *l'univers, Sciences de la Terre* 314, 1499–1506.

906 Eglinger A., André-Mayer A.-S., Combes V., Teitler Y., Heuret A., 2020. Les gisements d'or
907 de la Guyane française. *Géologues* 206 :36-40.

908 Enjolvy, R., 2008. Processus d'accrétion crustale et régimes thermiques dans le bouclier des
909 Guyanes: signatures géochimiques et thermochronologiques au transamazonien (2250-
910 1950Ma). PhD Thesis. Université Montpellier II-Sciences et Techniques du Languedoc,
911 pp. 305

912 Fougereuse, D., Micklethwaite, S., Tomkins, A.G., Mei, Y., Kilburn, M., Guagliardo, P.,
913 Fisher, L.A., Halfpenny, A., Gee, M., Paterson, D., Howard, D.L., 2016a. Gold
914 remobilisation and formation of high grade ore shoots driven by dissolution-reprecipitation
915 replacement and Ni substitution into auriferous arsenopyrite. *Geochimica et*
916 *Cosmochimica Acta* 178, 143–159.

917 Fougereuse D, Micklethwaite S, Ulrich S, Miller J, Godel B, Adams DT, McCuaig TC., 2017.
918 Evidence for two stages of mineralization in West Africa's largest gold deposit: Obuasi,
919 Ghana. *Econ Geol.* 112: 3–22.

920 Gapais, D., 2018. Tectonics-mineralisation relationships within weak continental lithospheres:
921 A new structural framework for Precambrian cratons. *BSGF-Earth Sci Bull.* 189. 14.
922 10.1051/bsgf/2018014.

923 Gébelin, A., Brunel, M., Monié, P., Faure, M., Arnaud, N., 2007. Transpressional tectonics and
924 Carboniferous magmatism in the Limousin, Massif Central, France: structural and
925 ⁴⁰Ar/³⁹Ar investigations. *Tectonics* 26, TC2008. doi:10.1029/2005TC001822.

926 Gerdes, A., Zeh, A., 2009. Zircon formation versus zircon alteration – New insights from
927 combined U-Pb and Lu-Hf in-situ La-ICP-MS analyses of Archean zircons from the
928 Limpopo Belt. *Chem. Geol.* 261. 230-243. 10.1016/j.chemgeo.2008.03.005.

929 Gibbs, A.K., Barron, C.N., 1993. *The Geology of the Guiana Shield.* Oxford University Press,
930 USA, pp. 246.

931 Groves, D.I., Goldfarb R.J., Gebre-Mariam, M., Hagemann S.G., Robert, F., 1998. Orogenic
932 gold deposits—a proposed classification in the context of their crustal distribution and
933 relationship to other gold deposit types. *Ore Geol. Rev.* 13, 7–27.

934 Groves, D.I., Santosh, M., Zhang, L., 2020b. A scale-integrated exploration model for orogenic
935 gold deposits based on a mineral system approach. *Geosci. Front.* 11 (3),719–738

936 Guineberteau, B., Bouchez, J.-L., Vignerresse, J.-L., 1987. The Mortagne granite pluton
937 (France) emplaced by pull-apart along shear zone: structural and gravimetric arguments
938 and regional implication. *Geol. Soc. Am. Bull.* 99, 763-770.

939 Hronsky, J.M.A., Groves, D.I., Loucks, R.R., Begg, G.C., 2012. A unified model for gold
940 mineralisation in accretionary orogens and implications for regional-scale exploration
941 targeting methods. *Miner. Depos.* 47, 339–358.

942 Hronsky, J.A., 2019. Deposit-scale structural controls on orogenic gold deposits: an integrated,
943 physical process-based hypothesis and practical targeting implications. *Miner. Depos.*
944 <https://doi.org/10.1007/s00126-019-00918z>.

945 Huston, D. L., Blewett, R. S. & Champion, D. C. 2012. Australia through time: a summary of
946 its tectonic and metallogenic evolution. *Episodes*, 35, 23–43.

947 Hutton, D. H. W., 1982. A tectonic model for the emplacement of the Main Donegal Granite,
948 NW Ireland, *J. Geol. Soc. London*, 139, 615 – 631

949 Irvine, T.N., Baragar, W.R.A., 1971. A Guide to the Chemical Classification of the Common
950 Volcanic Rocks. *Can. J. Earth Sci.* 8, 523-548

951 Jenkin, G., Lusty, P., Mcdonald, I., Smith, M., Boyce, A., Wilkinson, J., 2014. Ore deposits in
952 an evolving Earth: An introduction. *J. Geol. Soc. of London. Special Publications.* 393.
953 10.1144/SP393.14.

954 Jessell, M., Valenta, R.K., Jung, G., Cull, J.P., Geiro, A., 1993. Structural geophysics.
955 *Geophysics.* 24, 599–602.

956 Jessell, M.W. and Valenta, R.K., 1996, *Structural geophysics: Integrated structural and*
957 *geophysical modelling: Structural Geology and Personal Computers*, Elsevier Science Ltd,
958 Oxford, 303-324

959 Jessell MW, Begg GC, Miller MS. 2016. The geophysical signatures of the West African
960 Craton. *Precambrian Res* 274: 3–24.

961 Joly, A., Faure, M., Martelet, G., Chen, Y., 2009. Gravity inversion, AMS and geochronological
962 investigations of syntectonic granitic plutons in the southern part of the Variscan French
963 Massif Central. *J. Struct. Geol.* 31, 421-443.

964 Klaver, M., De Roever, E.W.F., Nanne, J.A.M., Mason, P.R.D., Davies, G.R., 2015.
965 Charnockites and UHT metamorphism in the Bakhuis Granulite Belt, western Suriname:
966 evidence for two separate UHT events. *Precamb. Res.* 262, 1–19.

967 Kreuzer, O. P., Buckingham, A., Mortimer, J., Walker, G., Wilde, A., Appiah, K., 2019. An
968 integrated approach to the search for gold in a mature, data-rich brownfields environment:
969 A case study from Sigma-Lamaque, Quebec. *Ore Geol. Rev.* 111, [102977].
970 <https://doi.org/10.1016/j.oregeorev.2019.102977>

971 Kroonenberg, S.B., de Roever, E.W.F., Fraga, L., Reis, N., Faraco, T., Lafon, J.-M., Cordani,
972 U., Wong, T., 2016. Paleoproterozoic evolution of the Guiana Shield in Suriname: a revised
973 model. *Neth. J. Geosci.* 95, 491–522.

974 Ledru, P., Laserre, J.L., Manier, E., Mercier, D., 1991. Le Proterozoïque inférieur nord
975 guyanais: révision de la lithologie, tectonique transcurrente et dynamique des bassins
976 sédimentaires. *Bull. Societ.* 162 (4), 627–636.

977 Lafrance, J., Bardoux, M., Voicu, G., Stevenson, R., Machado, N., 1999. Geological and
978 metallogenic environments of gold deposits of the Guiana Shield; a comparative study
979 between St-Elie (French Guiana) and Omai (Guyana). *Explor. Min. Geol.* 8, 117–135.

980 Large, R.R., Danyushevsky, L.V., Hollit, C., Maslennikov, V., Meffre, S., Gilbert, S., Bull, S.,
981 Scott, R., Emsbo, P., Thomas, H., and Foster, J., 2009, Gold and trace element zonation in
982 pyrite using a laser imaging technique: Implications for the timing of gold in orogenic and
983 Carlin-style sediment hosted deposits. *Econ Geol.* 104, 635–668.

984 Lasserre J.L., Ledru P., Manier E., Mercier D., 1989. Le Protérozoïque de Guyane. Révision
985 lithostructurale. Implications pour la formation détritique Orapu et la gîtologie de l'or.
986 Rapport BRGM 89 GUF023, 52 p.

987 Laurent, O., Björnsen, J., Wotzlav, J-F., Bretscher, S., Pimenta Silva, M., Moyen, J-F., Ulmer,
988 P., Bachmann, O., 2020. Earth's earliest granitoids are crystal-rich magma reservoirs
989 tapped by silicic eruptions. *Nat. Geosci.* 13. 1-7.

990 Martin, H., Smithies, R.H., Rapp, R.P., Moyen, J.-F., Champion, D.C., 2005. An overview of
991 adakite, tonalite–trondhjemite–granodiorite (TTG) and sanukitoid: relationships and some
992 implications for crustal evolution. *Lithos* 79, 1–24.

993

994 Metelka V, Baratoux L, Naba S, Jessell MW., 2011. A geophysically constrained litho-
 995 structural analysis of the Eburnean greenstone belts and associated granitoid domains,
 996 Burkina Faso, West Africa. *Precambr. Res.* 190: 48–69

997 McCuaig, T.C., Beresford, S., Hronsky, J., 2010. Translating the mineral systems approach into
 998 an effective exploration targeting system. *Ore Geol. Rev.* 38, 128–138.

999 McCuaig, T.C., Hronsky, J.M.A., 2014. The Mineral System Concept: the Key to Exploration
 1000 Targeting. *SEG 2014: Building Exploration Capability for the 21st Century*, pp. 153–175.

1001 Milesi, J., Lerouge C, Delór C, Ledru P, Billa M, Cocherie A, Egal E, Fouillac A, Lahondère
 1002 D, Lasserre J, Marot A, Martel-Jantin B, Rossi P, Tegye M, Théveniault H, Thiéblemont
 1003 D, Vanderhaeghe, O., 2003. Gold deposits (gold-bearing tourmalinites, gold-bearing
 1004 conglomerates, and mesothermal lodes), markers of the geological evolution of French
 1005 Guiana: geology, metallogeny, and stable isotope constraints. *Géol Fr*, 2-3-4:257-290.

1006 Miller, H.G., Singh, V., 1994. Potential field tilt—a new concept for location of potential field
 1007 sources. *J. Appl. Geophys.* 32, 213–217.

1008 Milligan, P.R., Gunn, P.J., 1997. Enhancement and presentation of airborne geophysical data.
 1009 *AGSO J. Aust. Geol. Geophys.* 17, 63–75.

1010 Motta, J. G., Souza Filho, C. R. d., Carranza, E. J. M., and Braitenberg, C., 2019, Archean crust
 1011 and metallogenic zones in the Amazonian Craton sensed by satellite gravity data: *Scientific*
 1012 *Reports*, v. 9, p. 2565

1013 Moyen, J.F., Martin, H., 2012. Forty years of TTG research. *Lithos*, 148, 312–336.

1014 Neves, S.P., Vauchez, A., Archanjo, C.J., 1996. Shear-zone controlled magma emplacement or
 1015 magma-assisted nucleation of shear zone? Insights from northeast Brazil. *Tectonophysics*
 1016 262, 349–364.

1017 Neves, S.P., Vauchez, A., Feraud, G., 2000. Tectono-thermal evolution, magma emplacement,
 1018 and shear zone development in the Caruaru area (Borborema Province, NE Brazil).
 1019 *Precambr. Res.* 99, 1–32.

1020 Neves, S.P., Marianoa, G., Beltrão, B.A., Correia, P.B., 2005. Emplacement and deformation
 1021 of the Cachoeirinha pluton (Borborema province, NE Brazil) inferred through
 1022 petrostructural studies: constraints on regional strain fields. *J. S. Am. Earth Sci.* 19, 127–
 1023 141.

- 1024 Niiranen, T., Nykänen, V., Lahti, I., 2019. Scalability of the mineral prospectivity modelling –
1025 An orogenic gold case study from northern Finland. *Ore Geol. Rev.* 109 :11-25.
- 1026 Nykänen, V., Lahti, I., Niiranen, T., Korhonen, K., 2015. Receiver Operating Characteristics
1027 (ROC) as validation tool for prospectivity models – a magmatic Ni-Cu case study from the
1028 Central Lapland greenstone belt, Northern Finland. *Ore Geol. Rev.* 71, 853–860.
- 1029 Norcross, C., Davis, D.W., Spooner, T.C., Rust, A., 2000. U/Pb and Pb/Pb age constraints on
1030 Paleoproterozoic magmatism, deformation and gold mineralization in the Omai area
1031 Guiana Shield. *Precamb. Res.* 102, 69–86.
- 1032 Parra-Avila LA, Belousova E, Fiorentini ML, Eglinger A, Block S, Miller J. 2018. Zircon Hf
1033 and O-isotope constraints on the evolution of the Paleoproterozoic Baoule-Mossi domain
1034 of the southern West African Craton. *Precambrian Res* 306: 174–188.
- 1035 Parra-Avila, L.A., Baratoux, L., Eglinger, A., Fiorentini, M.L., Block, S., 2019. The Eburnean
1036 magmatic evolution across the Baoulé-Mossi domain: Geodynamic implications for the
1037 West African Craton. *Precambrian Res.* 332, 105392. <https://doi.org/10.1016/j>
- 1038 Paterson, S. R., Fowler, T. K., 1993a. Re-examining pluton emplacement processes. *J. Struct.*
1039 *Geol.* 15, 191-206.
- 1040 Paterson, S.R., Schmidt, K.L., 1999. Is there a close spatial relationship between faults and
1041 plutons? *J. Struct. Geol.* 21, 1131-1142.
- 1042 Paterson, S.R., 2005. Close spatial relationship between plutons and shear zones: comment and
1043 reply. *Geology* 33 (1), 72.
- 1044 Pereira, M.F., Chichorro, M., Moita, P., Santos, J.F., Solá, A.M.R., Williams, I.S., Silva, J.B.,
1045 Armstrong, R.A., 2015. The multistage crystallization of zircon in calc-alkaline granitoids:
1046 U–Pb age constraints on the timing of Variscan tectonic activity in SW Iberia. *Int J Earth*
1047 *Sci.* 104 (5): 1167-1183.
- 1048 Perret, J., Eglinger, A., André-Mayer, A.-S., Aillères, L., Feneyrol, J., Hartshorne, C., Abanyin,
1049 E., Bosc, R., 2020. Subvertical, linear and progressive deformation related to gold
1050 mineralization at the Galat Sufar South deposit, Nubian Shield, NE Sudan. *Journal of*
1051 *Structural Geology* 135, 104032.
- 1052 Perrouty S, Ailleres L, Jessell MW, Baratoux L, Bourassa Y, Crawford B. 2012. Revised
1053 Eburnean geodynamic evolution of the gold-rich southern Ashanti Belt, Ghana, with new
1054 field and geophysical evidence of pre-Tarkwaian deformations. *Precambrian Res* 204: 12–
1055 39.

1056
1057 Phillips, G. N., Groves, D. I., 1983. The nature of Archaean gold-bearing fluids as deduced
1058 from gold deposits of Western Australia. *J Geol Soc Aust.* 30:1-2, 25-39
1059 Phillips, G.N., and Powell R., 2010, Formation of gold deposits: a metamorphic devolatilization
1060 model. *J Metam Geol.* 28, 689–718.
1061 Pilkington, M., Keating, P.B., 2009. The utility of potential field enhancements for remote
1062 predictive mapping. *Can. J. Remote Sens.* 35 (Suppl. 1), S1–S11.
1063 Pitcairn, I., Teagle, D.A.H., Craw, D., Olivo, G.R., Kerrich, R. and Brewer, T.S., 2006. Sources
1064 of metals and fluids in orogenic gold deposits: insights from the Otago and Alpine schists,
1065 New Zealand. *Econ Geol.* 101 (8), 1525-1546.
1066 Sánchez, M., Allan, M., Hart, C., Mortensen, J., 2014. Extracting ore-deposit-controlling
1067 structures from aeromagnetic, gravimetric, topographic, and regional geologic data in
1068 western Yukon and eastern Alaska. *Interpretation.* 2. SJ75-SJ102. 10.1190/INT-2014-
1069 0104.1.
1070 Shirey, S.B., Walker, R.J., 1995. Carius tube digestion for low-blank rhenium-osmium analysis.
1071 *Anal. Chem.* 67, 2136–2141.
1072 Siddorn, J. P., Williams, P. R., Isles, D. J., Rankin, L. R. 2020. Integrated Geologic-Geophysical
1073 Interpretation of District-Scale Structural Frameworks: Systematic Approaches for
1074 Targeting Mineralizing Systems. *Reviews in Econ. Geol.* 21, 271–313
1075 Stacey, J.S., Kramers, J.D., 1975. Approximation of terrestrial lead isotope evolution by a two-
1076 stage model. *Earth Planet. Sci. Lett.* 26, 207–221.
1077 Stewart, J. R., Betts, P. G., Collins, A. S., Schaefer, B. F., 2009. Multi-scale analysis of
1078 Proterozoic shear zones: An integrated structural and geophysical study. *J. Struct. Geol.*
1079 31(10), 1238-1254. <https://doi.org/10.1016/j.jsg.2009.07.002>
1080 Sun, S.S., and McDonough, W.F., 1989, Chemical and isotopic systematics of oceanic basalts:
1081 Implications for mantle composition and processes. *Geol. Soc. Spec. Publi* 42, 313–345.
1082 Tedeschi, M., Hagemann, S.G., Davis, J., 2018a. The Karouni Gold Deposit, Guyana, South
1083 America: part I. Stratigraphic Setting and Structural Controls on Mineralization. *Econ.*
1084 *Geol.* 113, 1679–1704.
1085 Thébaud, N., Sugiono, D., LaFlamme, C., Miller, J., Fisher, L., Voute, F., Tessalina, S.,
1086 Sonntag, I., & Fiorentini, M., 2018. Protracted and polyphased gold mineralisation in the
1087 Agnew District (Yilgarn Craton, Western Australia). *Precamb. Res.* 310, 291-304.

1088

1089 Théveniaut, H., Freyssinet, Ph., 2002. Timing of lateritization on the Guiana Shield: Synthesis
1090 of paleomagnetic results from French Guiana and Suriname. *Palaeogeogr. Palaeoclimatol.*
1091 *Palaeoecol.* 178. 91-117. 10.1016/S0031-0182(01)00404-7.

1092 Verduzco, B., Fairhead, J.D., Green, C.M., MacKenzie, C., 2004. New insights into magnetic
1093 derivatives for structural mapping. *The Leading Edge* 23, 116–119.

1094 Voicu, G., Bardoux, M., Jébrak, M., Crépeau, R., 1999. Structural, Mineralogical, and
1095 Geochemical Studies of the Paleoproterozoic Omai Gold Deposit, Guyana. *Econ. Geol.* 94,
1096 1277–1304.

1097 Voicu, G., Bardoux, M. and Stevenson, R. 2001. Lithostratigraphy, geochronology and gold
1098 metallogeny in the northern Guiana Shield, South America: a review. *Ore Geology*
1099 *Reviews*, 18, 211–236, [https://doi.org/ 10.1016/S0169-1368\(01\)00030-0](https://doi.org/10.1016/S0169-1368(01)00030-0)

1100 Völkening, J., Walczyk, T., Heumann, K.G., 1991. Osmium isotope determinations by negative
1101 thermal ionization mass spectrometry. *Int. J. Mass Spectrom.* 105, 147–159.

1102 Vanderhaeghe, O., Ledru, P., Thiéblemont, D., Egal, E., Cocherie, A., Tegye, M., Milési, J.-
1103 P., 1998. Contrasting mechanism of crustal growth: Geodynamic evolution of the
1104 Paleoproterozoic granite–greenstone belts of French Guiana. *Precambr. Res.* 92, 165–193.

1105 Weinberg, R.F., Sial, A.N., Mariano, G., 2004. Close spatial relationship between plutons and
1106 shear zones. *Geology* 32 (5), 377-380.

1107 Wyborn, L.A.I., Heinrich, C.A., Jaques, A.L., 1994. Australian Proterozoic Mineral Systems:
1108 Essential Ingredients and Mappable Criteria. Australasian Institute of Mining and
1109 Metallurgy Annual Conference, Melbourne, pp. 109–115.

1110 Wyman, D.A., Cassidy, K.F., Hollings, P., 2016. Orogenic gold and the mineral
1111 systems approach: resolving fact, fiction and fantasy. *Ore Geol. Rev.* 78, 322–335.

1112

1113

1114

1115

1116

1117

1118

1119 **Captions**

1120

1121 Figure 1 Geology of the Guiana Shield (modified from Kroonenberg et al., 2016). Gold deposits
1122 presented have total resources > 10 Moz. MKSZ: Makapa-Kuribrong Shear Zone, NGT:
1123 Northern Guiana Trough, CGSZ: Central Guiana Shear Zone. Geographic coordinates are
1124 reported as WGS 84.

1125

1126 Figure 2 Geological map of French Guiana with location of the main Au deposits including the
1127 Yaou deposit. Modified from Delor et al. (2003b). All geochronology data are from Delor et al.
1128 (2003b) and references therein.

1129

1130 Figure 3 Regional geological map with location of the main Au occurrences. Modified from
1131 Delor et al. (2003b), mainly based on geophysical interpretation of the regional BRGM survey.
1132 See Figure 2 for location.

1133

1134 Figure 4 Schematic 3D block diagram of the deposit at the camp-scale after all deformation/
1135 intrusion events occurred, highlighting the geometry of the CYSZ associated with the D_{3YA}
1136 deformation phase and the pre to syn- D_{3YA} intrusive bodies

1137

1138 Figure 5 Leapfrog Geo scene of the model with orebodies geometry at the camp-scale (central
1139 part of the deposit). Orebodies associated with D_{4YA} correspond to intrusive bodies enveloppes.
1140 See Fig. 4 for location.

1141

1142 Figure 6 Photographs of half-drillcore intervals presenting the least altered samples of the
1143 quartz monzodiorite intrusive bodies.

1144

1145 Figure 7 Representative micrographs of the least altered quartz monzodiorite (XPL except F. in
1146 PPL) A. B. D Typical albitization and seritization, C. E. Strong ankeritization. F. Hematization

1147 along albite grains. Abbreviations: Albite (Ab), Quartz (Qz), Ankerite (Ank), Sericite (Ser),
1148 Chlorite (Chl), Pyrite (Py), Hematite (Hem), K-feldspar (Kf).

1149

1150 Figure 8 A. QAP Streckeis ternary diagram where all samples plot in the Qz monzodiorite
1151 field. B. Least altered samples plotted in a Th vs Co diagram. C. Ternary An-Ab-Or diagram
1152 (Barker, 1979). D. REE abundances normalized to chondritic values from Sun and McDonough
1153 (1989). E. Spider plot normalized to primitive mantle values from Sun and McDonough (1989).

1154

1155 Figure 9 Yaou Quartz monzodiorite REE Normalized to Chondrite (Sun and McDonough,
1156 1989) patterns compared to the main intrusive units defined in French Guiana. A. The "Ile de
1157 Cayenne" Complex patterns. B. The 1st generation of TTG-like patterns. C. The 2nd generation
1158 of TTG-like patterns. D. The late samples of the 2nd generation of TTG-like patterns. E. The
1159 Ganitic suite patterns. F. The peraluminous leucogranite patterns. Compared geochemical data
1160 are from Vanderhaeghe et al. (1998), Delor et al. (2003a, b) and Enjolvy (2008).

1161

1162 Figure 10 A. BSE images of representative analysed zircon grains from the quartz monzodiorite
1163 intrusion. The circles indicate Lu-Hf and U-Pb laser spots. The numbers are respectively the
1164 sample ID, the $^{207}\text{Pb}/^{206}\text{Pb}$ age and the Hf model age of the corresponding spot. B. $^{207}\text{Pb}/^{235}\text{U}$
1165 versus $^{206}\text{Pb}/^{238}\text{U}$ diagrams for the quartz monzodiorite (intercept). C. $^{207}\text{Pb}/^{235}\text{U}$ versus
1166 $^{206}\text{Pb}/^{238}\text{U}$ diagrams for the quartz monzodiorite (concordance). D. ϵHf_t as a function of
1167 intrusion age (Ma). Crustal evolution trends (between dotted lines) are calculated with a value
1168 of $^{176}\text{Lu}/^{177}\text{Hf} = 0.0113$, value for average present-day continental crust. Stars at the intersection
1169 of depleted mantle and crustal evolution trends represent Hafnium model ages. CHUR =
1170 chondritic uniform reservoir; DM = depleted mantle.

1171

1172 Figure 11 Lithological interpretations based on airborne geophysics. A. K anomaly grid used
1173 to map the metasedimentary unit. B. U anomaly map highlighting the U-rich TTG-like
1174 complex. C. Ternary radio-element map (relative abundance) of K, Th and U. D. 1VD image
1175 emphasizing shallow features. E. Overview of the interpreted distribution of lithologies at the
1176 district-scale

1177

1178 Figure 12 Structural interpretation using airborne geophysics A. Aeromagnetic map with RTP-
1179 TD grid enhancing magnetic lineaments. B. Aeromagnetic map with RTP-TD-HRD grid
1180 showing maximum ridges over edges of magnetic bodies. C. Aeromagnetic map with 1VD
1181 displaying magnetic intensity with color gradient. D. Overview of main structures identified at
1182 the district-scale overlain over shaded DTM.

1183

1184 Figure 13 Geochronological synthesis of the Trans-Amazonian orogeny with deformation
1185 phases (Delor et al., 2003 a, b), compilation of published geochronological data of main
1186 plutonic events (zircon Pb/Pb and U-Pb; Vanderhaeghe et al., 1998; Delor et al., 2003b; Enjolvy
1187 2008) and interpreted integration of the Yaou camp-scale deformation phases from Re-Os
1188 dating on pyrite (Py₄) and U-Pb dating on zircon (quartz monzodiorite i.e. intrusive event) in
1189 the regional framework.

1190

1191

1192

1193 Figure 14 Structural interpretation of the distribution of faults, shear zones and intrusive bodies
1194 A. High to low magnetic response in greyscale (RTP TD filter). B. Geophysical-based structural
1195 and lithological interpretations displaying the proposed intrusive body trends, a serie of N60°-
1196 striking shear zones (in low magnetic responses areas) and late D_{4YA}- related faults interpreted
1197 using the TD-HDR filter. High magnetic response may correspond to a dipping stratigraphy or
1198 folded stratigraphy with horizontal fold axes.

1199

1200 Figure 15 Sketches illustrating the structural settings at the camp-scale. A. The Pre-D_{3YA} phase.
1201 B. The syn-D_{3YA} shearing contemporaneous with the intrusive body. C. 3D representation of
1202 the interpreted shearing induced intrusive event with two hypotheses of formation, tension
1203 gashes or backfolding of fabric. D. Structural overview of the C/S₃ fabrics (associated with the
1204 D_{3YA} deformation phase) and the spatial relationship S₂ fabrics (associated with the D_{2YA}
1205 deformation phase).

1206

1207 Figure 16 A. Litho-structural map produced from geological and geophysical data at the district-
 1208 scale. B. Cross section of Delor et al.(2003b) through the Yaou district vs the updated cross-
 1209 section from this study with two separated plutons.

1210

1211

1212

1213

1214

1215

1216

1217

1218 **Tables**

1219

1220 Table 1. Whole rock major (wt.%) and trace element (ppm) composition of sampled intrusive
 1221 rocks (dl, detection limit)

1222

1223

ID	SiO ₂ (wt.%)	Al ₂ O ₃	Fe ₂ O ₃	MnO	MgO	CaO	Na ₂ O	K ₂ O	TiO ₂	P ₂ O ₅	LOI
F69	64.07	16.09	4.66	0.02	1.63	1.21	5.91	3.55	0.64	0.23	1.79
F03	68.48	15.56	2.35	0.03	0.64	1.30	7.42	1.55	0.28	0.14	2.40
F20-147.3	61.76	16.30	4.55	0.02	1.99	1.80	6.52	3.24	0.62	0.21	2.93
F20-145.3	64.71	15.22	4.36	0.04	1.78	2.23	6.67	1.58	0.58	0.2	2.77
F20-01	64.27	15.15	4.15	0.05	1.5	3.18	5.61	1.96	0.58	0.19	3.98
dl	0.05	0.04	0.02	0.02	0.03	0.03	0.02	0.03	0.02	0.10	

ID	As (ppm)	Ba	Be	Bi	Cd	Co	Cr	Cs	Cu	Ga	Ge
F69	1.93	483	1.62	0.33	0.06	9.06	17.30	0.26	43.30	21.80	1.11
F03	1.66	682	1.39	0.50	0.21	2.64	2.30	0.17	19.40	20.30	1.10
F20-147.3	1.38	353	1.36	0.58	0.04	9.70	20.30	0.07	43.90	20.90	1.10
F20-145.3	0.74	455	1.30	0.13	0.06	8.84	18.90	0.11	38.40	21.40	1.13
F20-01	0.57	807	1.10	0.17	0.05	8.83	14.30	0.40	6.19	22.29	1.21
dl	0.50	5.50	0.05	0.05	0.02	0.08	0.50	0.02	2.00	0.02	0.04

ID	Hf	In	Mo	Nb	Ni	Pb	Rb	Sb	Sc	Sn	Sr
F69	4.05	0.03	<dl	7.63	12.00	8.10	46.20	0.50	7.84	3.53	236.00
F03	3.77	<dl	3.76	5.55	<dl	8.76	22.10	1.22	2.89	1.59	350.00
F20-147.3	4.48	<dl	3.49	8.41	13.20	7.97	39.60	0.38	6.11	1.70	356.00
F20-145.3	3.88	0.03	<dl	7.77	12.20	13.90	20.40	0.24	7.48	2.36	336.00
F20-01	3.95	0.03	<dl	7.49	10.63	12.82	41.01	0.25	7.15	1.33	346.50
dl	0.03	0.03	0.50	0.02	2.00	0.45	0.15	0.06	0.60	0.30	0.70

ID	Ta	Th	U	V	W	Y	Zn	Zr	La	Ce	Pr
----	----	----	---	---	---	---	----	----	----	----	----

F69	0.61	5.42	1.47	91.50	6.17	10.2	64.70	156.00	31.70	64.10	7.75
F03	0.51	6.23	1.86	38.90	6.85	5.78	38.40	151.00	29.50	55.10	6.18
F20-147.3	0.72	6.18	1.50	99.00	7.42	9.35	59.40	162.00	33.90	70.80	8.27
F20-145.3	0.65	5.23	1.58	89.90	5.50	10.80	61.50	143.00	28.20	57.80	7.02
F20-01	0.60	5.16	1.65	69.27	10.94	10.44	70.96	144.10	30.14	64.59	7.22
dl	0.01	0.02	0.01	0.85	0.80	0.02	7.00	1.50	0.02	0.03	0.01

ID	Nd	Sm	Eu	Gd	Tb	Dy	Ho	Er	Tm	Yb	Lu	Total
F69	29.70	5.23	1.41	3.53	0.43	2.20	0.40	1.02	0.14	0.88	0.13	99.81
F03	22.10	3.37	0.95	2.12	0.24	1.19	0.21	0.55	0.08	0.52	0.07	100.15
F20-147.3	31.20	5.41	1.40	3.68	0.43	2.10	0.37	0.92	0.13	0.82	0.12	99.93
F20-145.3	27.10	4.89	1.30	3.41	0.43	2.24	0.41	1.06	0.15	0.92	0.13	100.11
F20-01	26.89	4.64	1.28	3.32	0.42	2.21	0.41	1.03	0.14	0.88	0.13	100.62
dl	0.02	0.01	0.01	0.01	0.01	0.01	0.01	0.01	0.01	0.01	0.01	0.01

1224

Table 2 Results of U-Pb-dating.

Grain ID	²⁰⁷ Pb ^a	U ^b	Pb ^b	Th ^b	²⁰⁶ Pb ^c	²⁰⁶ Pb ^d	±2s	²⁰⁷ Pb ^d	±2s	²⁰⁷ Pb ^d	±2s	rho ^e	²⁰⁶ Pb	±2s	²⁰⁷ Pb	±2s	²⁰⁷ Pb	±2s	conc. ^f
	(cps)	(ppm)	(ppm)	U	(%)	²³⁸ U	(%)	²³⁵ U	(%)	²⁰⁶ Pb	(%)		²³⁸ U	(Ma)	²³⁵ U	(Ma)	²⁰⁶ Pb	(Ma)	(%)
a251	281477	470	208	0,49	0,29	0,39310	2,9	7,2	3,0	0,1328	0,7	0,97	2137	53	2136	27	2136	12	100
a252	87414	148	66	0,65	0,52	0,39190	2,5	7,142	2,6	0,1322	0,6	0,97	2132	46	2129	24	2127	10	100
a253	79490	135	61	0,68	0,24	0,39470	2,6	7,203	2,6	0,1324	0,5	0,98	2144	47	2137	24	2130	9	101
a254	322633	516	226	0,41	0,30	0,39260	2,7	7,141	2,7	0,1319	0,6	0,98	2135	49	2129	25	2124	10	101
a255	451003	745	310	0,20	0,10	0,39360	2,7	7,233	2,7	0,1333	0,3	0,99	2140	49	2141	24	2141	6	100
a256	206533	347	151	0,47	0,64	0,38950	2,9	7,08	3,1	0,1318	1	0,94	2121	52	2121	28	2122	18	100
a257	88528	145	58	0,01	0,01	0,39210	2,6	7,135	2,6	0,132	0,4	0,99	2133	47	2128	24	2124	8	100
a258	238939	482	207	0,74	0,85	0,37930	4,9	6,815	5,0	0,1303	1,2	0,97	2073	87	2088	45	2102	21	99
a259	259355	476	215	0,58	0,11	0,39240	2,9	7,152	3,0	0,1322	0,8	0,97	2134	53	2131	27	2127	13	100
a260	253835	502	218	0,50	0,26	0,39060	3,9	7,194	3,9	0,1336	0,4	1,00	2126	70	2136	35	2145	6	99
a261	266534	442	197	0,65	1,91	0,37850	2,7	6,853	3,1	0,1313	1,6	0,85	2069	47	2093	28	2116	29	98
a262	241511	377	147	0,51	0,44	0,34150	2,7	6,101	2,9	0,1296	1	0,94	1894	45	1990	26	2092	18	91
a263	215892	450	196	0,44	0,36	0,39070	3,4	7,096	3,6	0,1317	1,1	0,95	2126	62	2124	32	2121	20	100
a264	232006	481	211	0,50	0,85	0,38650	3,1	6,941	3,3	0,1302	1,1	0,94	2107	55	2104	29	2101	20	100
a265	274751	551	243	0,45	0,31	0,39340	2,6	7,175	2,8	0,1323	1,1	0,92	2139	47	2133	25	2128	19	100
a266	300304	541	240	0,52	0,26	0,39150	2,7	7,107	2,8	0,1316	0,6	0,98	2130	50	2125	25	2120	11	100
a267	175230	351	153	1,16	0,60	0,39110	3,0	7,128	3,2	0,1322	1,2	0,93	2128	54	2127	29	2127	20	100
a268	96299	164	78	0,93	0,48	0,39510	2,5	7,234	2,6	0,1328	0,6	0,97	2146	46	2141	23	2135	10	101
a269	162528	265	112	0,35	b.d.	0,39140	2,5	7,164	2,7	0,1328	0,9	0,94	2129	46	2132	24	2135	16	100
a270	236969	405	178	0,59	0,48	0,38920	3,2	7,067	3,3	0,1317	0,6	0,98	2119	58	2120	30	2121	11	100

Spot size = 33µm. ²⁰⁶Pb/²³⁸U error is the quadratic additions of the within run precision (2 SE) and the external reproducibility (2 SD) of the reference zircon. ²⁰⁷Pb/²⁰⁶Pb error propagation (²⁰⁷Pb signal dependent) following Gerdes & Zeh (2009). ²⁰⁷Pb/²³⁵U error is the quadratic addition of the ²⁰⁷Pb/²⁰⁶Pb and ²⁰⁶Pb/²³⁸U uncertainty.

^a Within run background-corrected mean ²⁰⁷Pb signal in cps (counts per second).

^b U and Pb content and Th/U ratio were calculated relative to GJ-1 reference zircon.

^c percentage of the common Pb on the ²⁰⁶Pb. B.d. = below detection limit.

^d corrected for background, within-run Pb/U fractionation (in case of ²⁰⁶Pb/²³⁸U) and common Pb using Stacy and Kramers (1975) model Pb composition and subsequently normalized to GJ-1 (ID-TIMS value/measured value); ²⁰⁷Pb/²³⁵U calculated using ²⁰⁷Pb/²⁰⁶Pb/(²³⁸U/²⁰⁶Pb*1/137.88)

^e rho is the 206Pb/238U/207Pb/235U error correlation coefficient.

^f degree of concordance = ²⁰⁶Pb/²³⁸U age / ²⁰⁷Pb/²⁰⁶Pb age x 100

Table 3 LA-ICPMS Lu-Hf isotope data of zircon.

Sample ID	$^{176}\text{Yb}/^{177}\text{Hf}$ a	$\pm 2s$	$^{176}\text{Lu}/^{177}\text{Hf}$ a	$\pm 2s$	$^{178}\text{Hf}/^{177}\text{Hf}$	$^{179}\text{Hf}/^{177}\text{Hf}$	Sig _{Hf} b	$^{176}\text{Hf}/^{177}\text{Hf}$ c	$\pm 2s$	$^{176}\text{Hf}/^{177}\text{Hf}_{(t)}$ ^d	eHf _(t) ^d	$\pm 2s$ c	T _{DM2} ^e	age ^f	$\pm 2s$	conc. ^g
							(V)						(Ga)	(Ma)		
a251	0,0378	13	0,00126	4	1,46729	0,74026	9	0,281554	28	0,281503	2,8	1,0	2,50	2127	6	100
a252	0,0032	3	0,00008	1	1,46723	0,74022	10	0,281463	27	0,281460	1,3	0,9	2,59	2127	6	100
a253	0,0244	10	0,00075	2	1,46726	0,74007	8	0,281521	26	0,281491	2,4	0,9	2,53	2127	6	100
a254	0,0325	9	0,00098	2	1,46726	0,74015	9	0,281529	32	0,281490	2,3	1,1	2,53	2127	6	100
a255	0,0394	11	0,00113	2	1,46724	0,74015	10	0,281542	30	0,281496	2,6	1,1	2,52	2127	6	100
a256	0,0375	18	0,00110	4	1,46725	0,74021	10	0,281577	26	0,281532	3,8	0,9	2,45	2127	6	100
a257	0,0343	9	0,00103	3	1,46731	0,74015	11	0,281552	37	0,281511	3,1	1,3	2,49	2127	6	100
a258	0,0374	11	0,00108	1	1,46726	0,74013	9	0,281550	29	0,281507	2,9	1,0	2,50	2127	6	100
a259	0,0325	5	0,00096	1	1,46727	0,74021	9	0,281546	30	0,281507	3,0	1,1	2,50	2127	6	100
a260	0,0422	39	0,00116	9	1,46733	0,74017	9	0,281588	34	0,281541	4,2	1,2	2,43	2127	6	100
a261	0,0344	14	0,00102	3	1,46728	0,74016	10	0,281555	28	0,281514	3,2	1,0	2,48	2127	6	100
a262	0,0301	9	0,00092	2	1,46727	0,74020	8	0,281552	26	0,281514	3,2	0,9	2,48	2127	6	100
a263	0,0360	32	0,00096	6	1,46726	0,74022	9	0,281558	37	0,281519	3,4	1,3	2,47	2127	6	100
a264	0,0280	14	0,00077	4	1,46725	0,74025	9	0,281530	31	0,281499	2,7	1,1	2,51	2127	6	100
a265	0,0349	18	0,00099	3	1,46726	0,74028	10	0,281559	26	0,281519	3,4	0,9	2,47	2127	6	100
a266	0,0639	28	0,00167	6	1,46730	0,74016	9	0,281572	32	0,281504	2,9	1,1	2,50	2127	6	100
a267	0,0509	15	0,00133	4	1,46725	0,74004	8	0,281543	29	0,281489	2,3	1,0	2,53	2127	6	100

(a) $^{176}\text{Yb}/^{177}\text{Hf} = (^{176}\text{Yb}/^{173}\text{Yb})_{\text{true}} \times (^{173}\text{Yb}/^{177}\text{Hf})_{\text{meas}} \times (M_{173(\text{Yb})}/M_{177(\text{Hf})})^{b(\text{Hf})}$, $b(\text{Hf}) = \ln(^{179}\text{Hf}/^{177}\text{Hf}_{\text{true}} / ^{179}\text{Hf}/^{177}\text{Hf}_{\text{measured}}) / \ln(M_{179(\text{Hf})}/M_{177(\text{Hf})})$, M=mass of respective isotope. The $^{176}\text{Lu}/^{177}\text{Hf}$ were calculated in a similar way by using the $^{175}\text{Lu}/^{177}\text{Hf}$ and b(Yb). Quoted uncertainties (absolute) relate to the last quoted figure. The effect of the inter-element fractionation on the Lu/Hf was estimated to be about 6 % or less based on analyses of the GJ-1 and Plesoviče zircons.

(b) Mean Hf signal in volt.

(c) Uncertainties are quadratic additions of the within-run precision and the daily reproducibility of the zircon GJ-1. Uncertainties for GJ-1 is 2SD (2 standard deviation).

(d) Initial $^{176}\text{Hf}/^{177}\text{Hf}$ and eHf calculated using the age (Ma), and the CHUR parameters: $^{176}\text{Lu}/^{177}\text{Lu} = 0.0336$, and $^{176}\text{Hf}/^{177}\text{Hf} = 0.282785$ (Bouvier et al., 2008).

(e) two stage model age in billion years using the measured $^{176}\text{Lu}/^{177}\text{Lu}$, the estimated age (Ma), a value of 0.01113 for the average continental crust (second stage), and a depleted mantle $^{176}\text{Lu}/^{177}\text{Hf}$ and $^{176}\text{Hf}/^{177}\text{Hf}$ of 0.03933 and 0.283294 (Blichert-Toft & Puchtel, 2010).

(f) $^{206}\text{Pb}/^{238}\text{U}$ age for zircon <1.0 Ga, and $^{206}\text{Pb}/^{207}\text{Pb}$ age for zircon >1.0 Ga. *-intrusion age

(g) degree of concordance (for detrital grains)

Table 4. The Re-Os data obtained on Py₄ pyrite

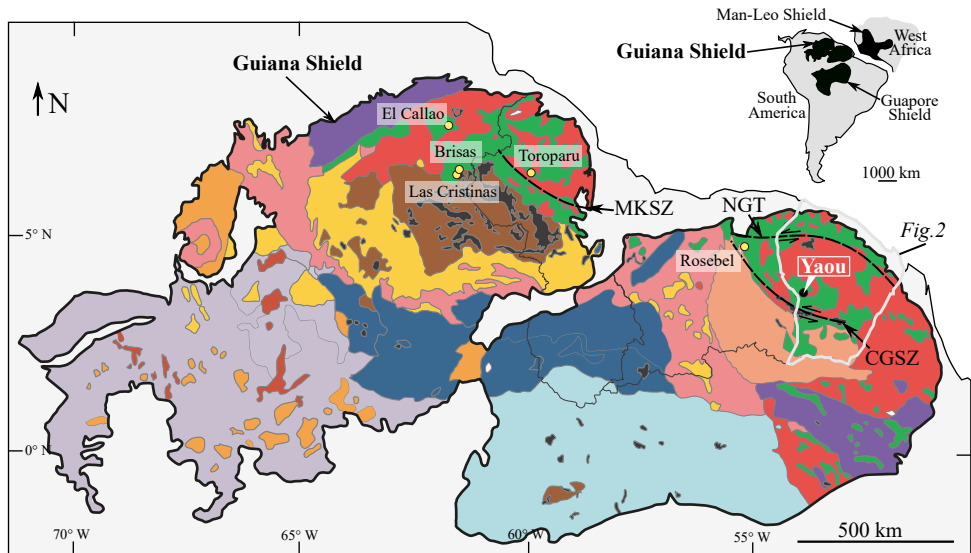
Name	Sample wt. (g)	[Re] ppb	total uncertainty	¹⁸⁷ Re M/g	total uncertainty	¹⁸⁸ Os M/g	% ¹⁸⁸ Os from blank
Yaou (1)	0.20292	26.57	0.3789	8.93E-11	1.27E-12	5.49E-15	22.9
Yaou (2)	0.20165	26.16	0.2037	8.80E-11	6.74E-13	5.69E-15	22.4

Name	¹⁸⁷ Os ppb blank corr	¹⁸⁷ rad if ¹⁸⁷ / ¹⁸⁸ (initial) =0.6	Total uncertainty	¹⁸⁷ Os/ ¹⁸⁸ Re	¹⁸⁷ Os/ ¹⁸⁷ Re uncertainty	Age (Ga)	Uncertainty
Yaou (1)	0.595	3.18E-12	6.50E-15	3.58E-02	5.15E-04	2.11	0.03
Yaou (2)	0.584	3.12E-12	6.00E-15	3.56E-02	2.83E-04	2.101	0.017

All data are blank corrected.

Radiogenic Os is estimated assuming an initial ¹⁸⁷Os/¹⁸⁸Os = 0.6 ± 0.5

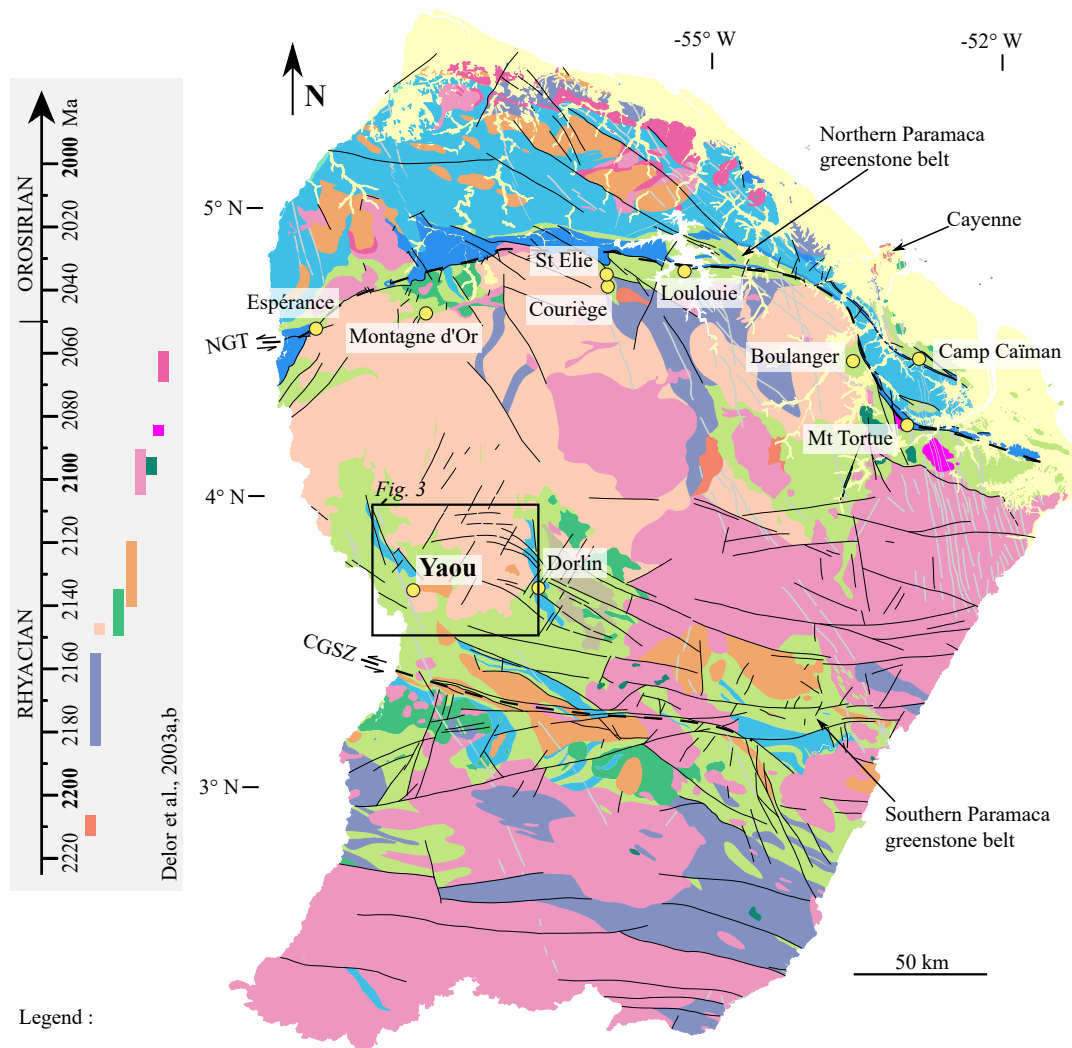
Total uncertainties (2 sigma) include measurement uncertainties, uncertainty on the blank reproducibility, and assumed variation in initial ¹⁸⁷Os/¹⁸⁸Os ratio.



Legend :

- | | |
|---|--|
| Younger platform covers (1.3-1.2 Ga) | Greenstone belt (2.26-2.09 Ga) |
| Mesoproterozoic intrusives (1.59-1.51 Ga) | Late intrusions |
| Rio Negro Belt (1.86-1.72 Ga) | TTG-like intrusions |
| Younger felsic volcanic and granitoid belt (1.89-1.81 Ga) | Volcano-sedimentary formations |
| Mafic intrusives (1.79 Ga and younger) | Archean nuclei (> 2.5 Ga) |
| Older platform Cover (1.87 Ga) | Au deposits (Resources > 10 Moz) |
| Older felsic volcanic and granitoid belt (1.86-1.72 Ga) | Main shear zones |
| High-grade belts (2.08-2.02 and ca. 1.98 Ga) | |

Fig 1 Color, 2-column fitting image.



Legend :

- | | |
|--|---|
| Quaternary sediments | Mafic complexes (2098-2093 Ma) |
| Dolerite (198-189 Ma, 808 Ma, 1800-1900 Ma) | TTG-like 2 nd generation (2140-2120 Ma) |
| Rhyolites (late Trans-Amazonian) | Mafic to ultramafic complexes (2149-2135 Ma) |
| D _{2a} -related Upper Detrital Unit | Granodioritic gneiss (2152-2144 Ma) |
| Lower Volcanic and Sedimentary Unit | |
| Metavolcanites (Paramaca greenstone belt) | TTG-like 1 st generation (2183-2155 Ma) |
| Metasediments (Paramaca greenstone belt) | "Ile de Cayenne" Complex Amphibolites/gabbros & Trondhjemite (2216-2208 Ma) |
| Magmatism | |
| Late metaluminous plutonism (2069-2060 Ma) | Main gold deposits |
| Peraluminous leucogranite (2092-2078 Ma) | Major faults |
| Granitic suite (2105-2090 Ma) | Major shear zones (NGT & CGSZ) |

Fig 2 Color, 2-column fitting image.

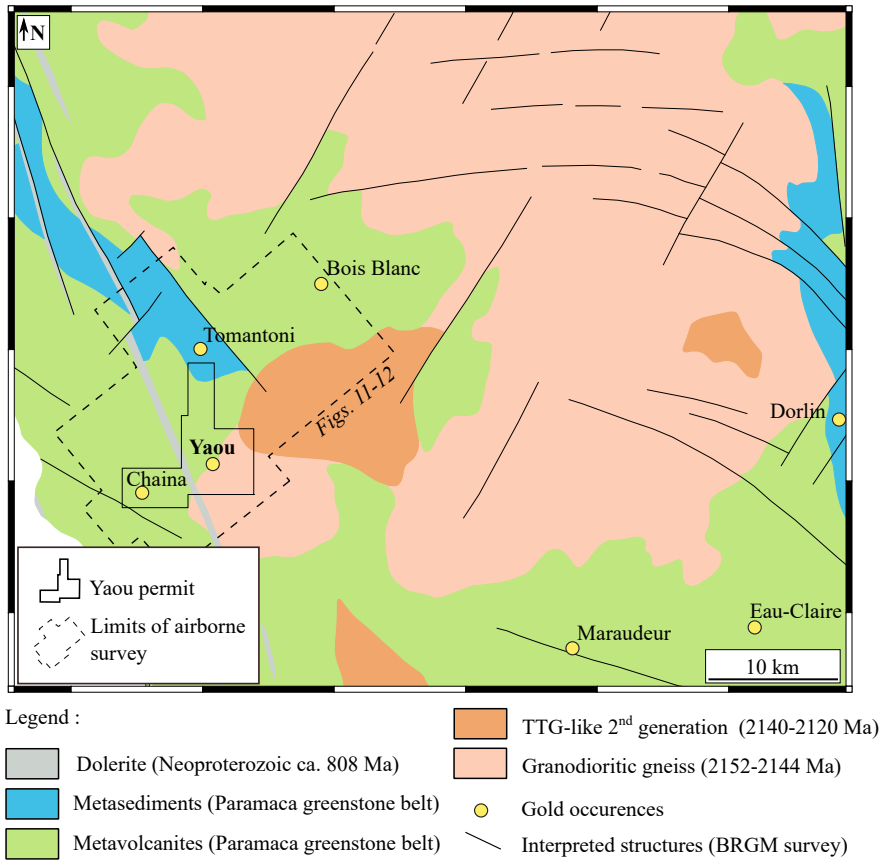
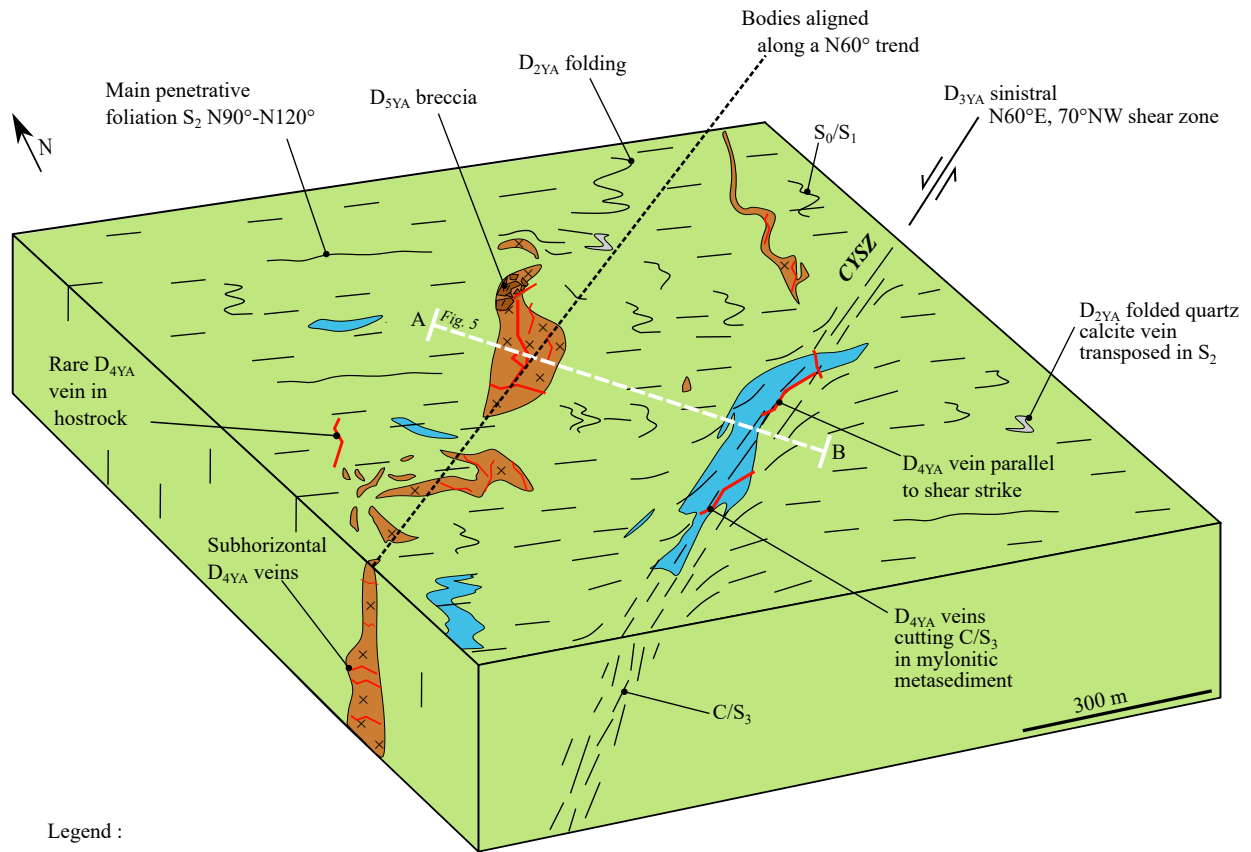


Fig 3 Color, 2-column fitting image.



Legend :

- | | | | | | | |
|---|---|---|-------------------|---|------------------|---|
|  | Pre to syn- D_{3YA} quartz monzodiorite |  | D_{5YA} breccia |  | C/S_3 fabric |  Central Yaou Shear Zone |
|  | Metasediments (Paramaca greenstone belt) |  | D_{4YA} vein |  | S_2 fabric | |
|  | Metavolcanites (Paramaca greenstone belt) |  | D_{2YA} vein |  | S_0/S_1 fabric | |

Fig 4 Color, 2-column fitting image.

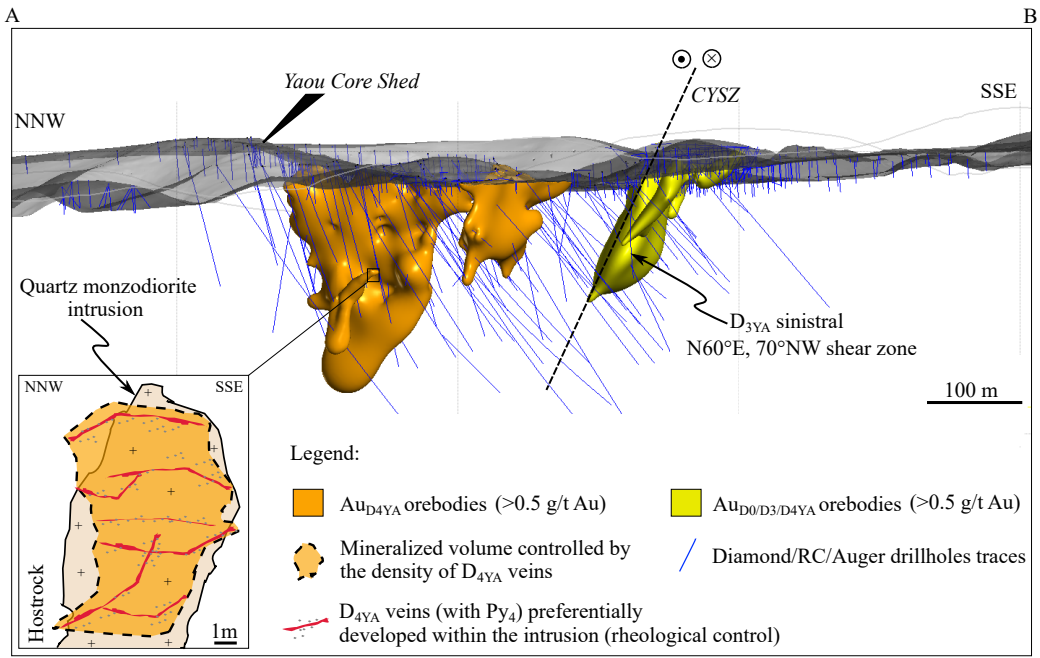


Fig 5 Color, 2-column fitting image.

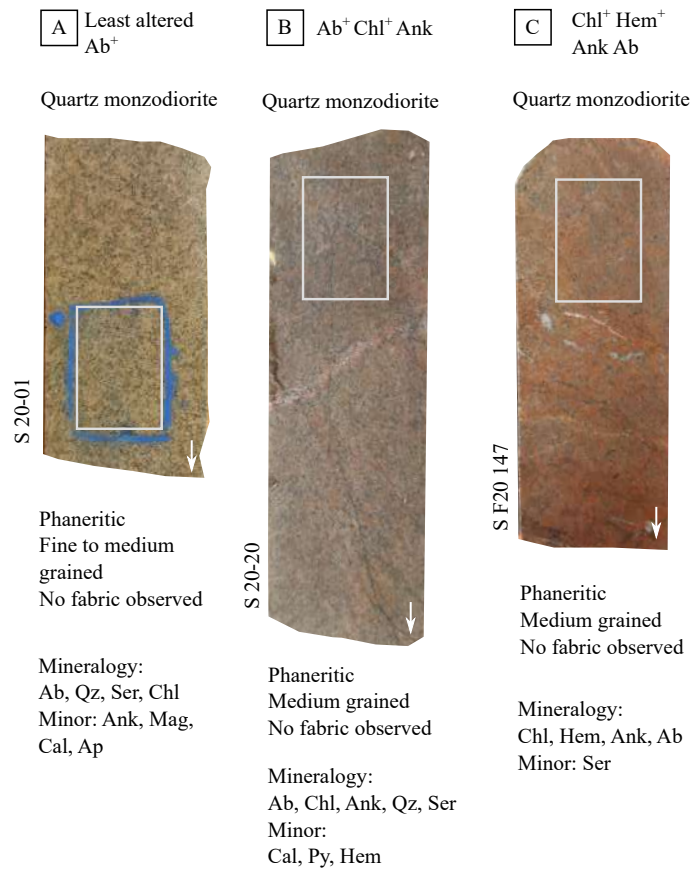


Fig 6 Color, 2-column fitting image.

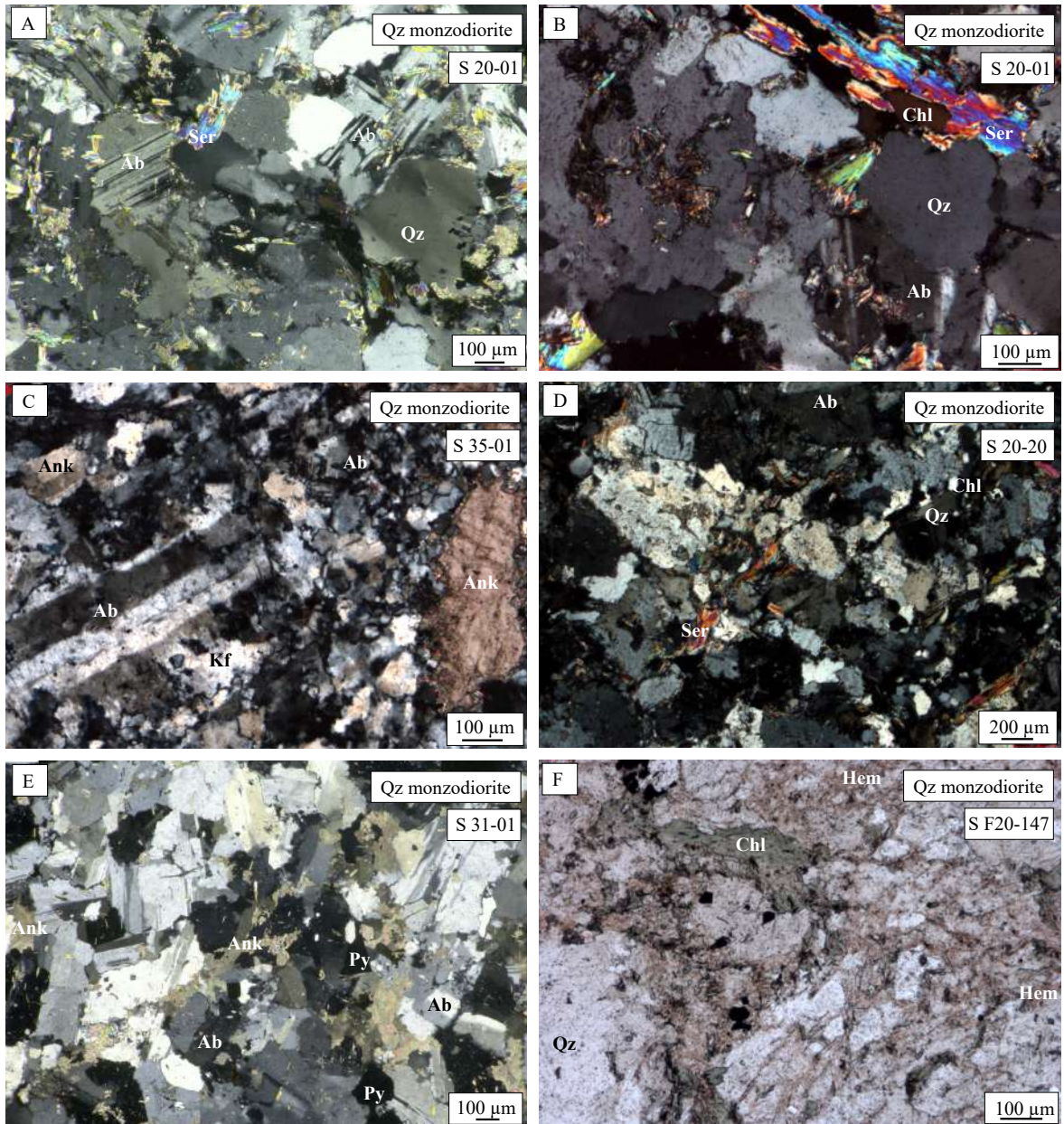


Fig 7 Color, 2-column fitting image.

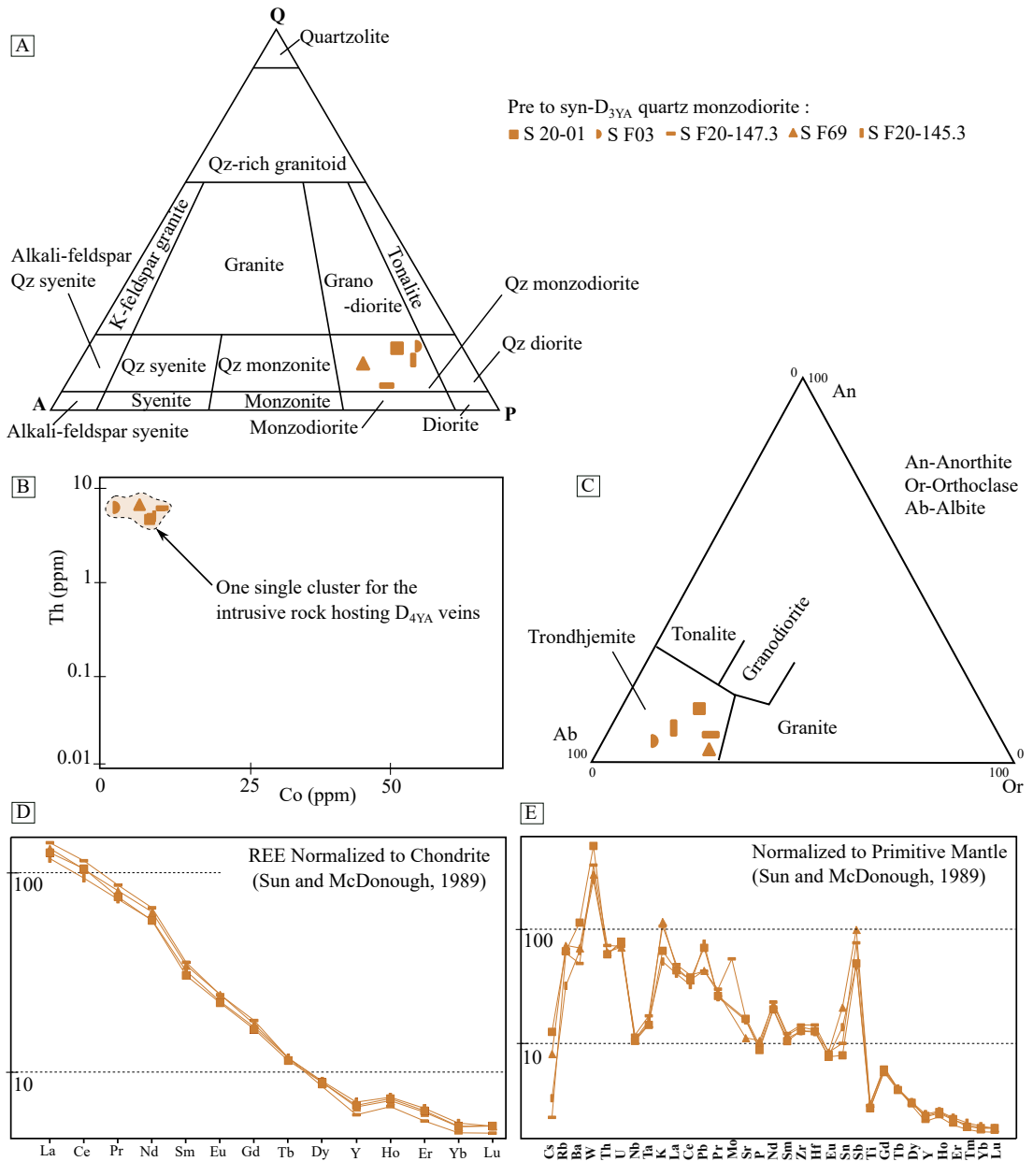


Fig 8 Color, 2-column fitting image.

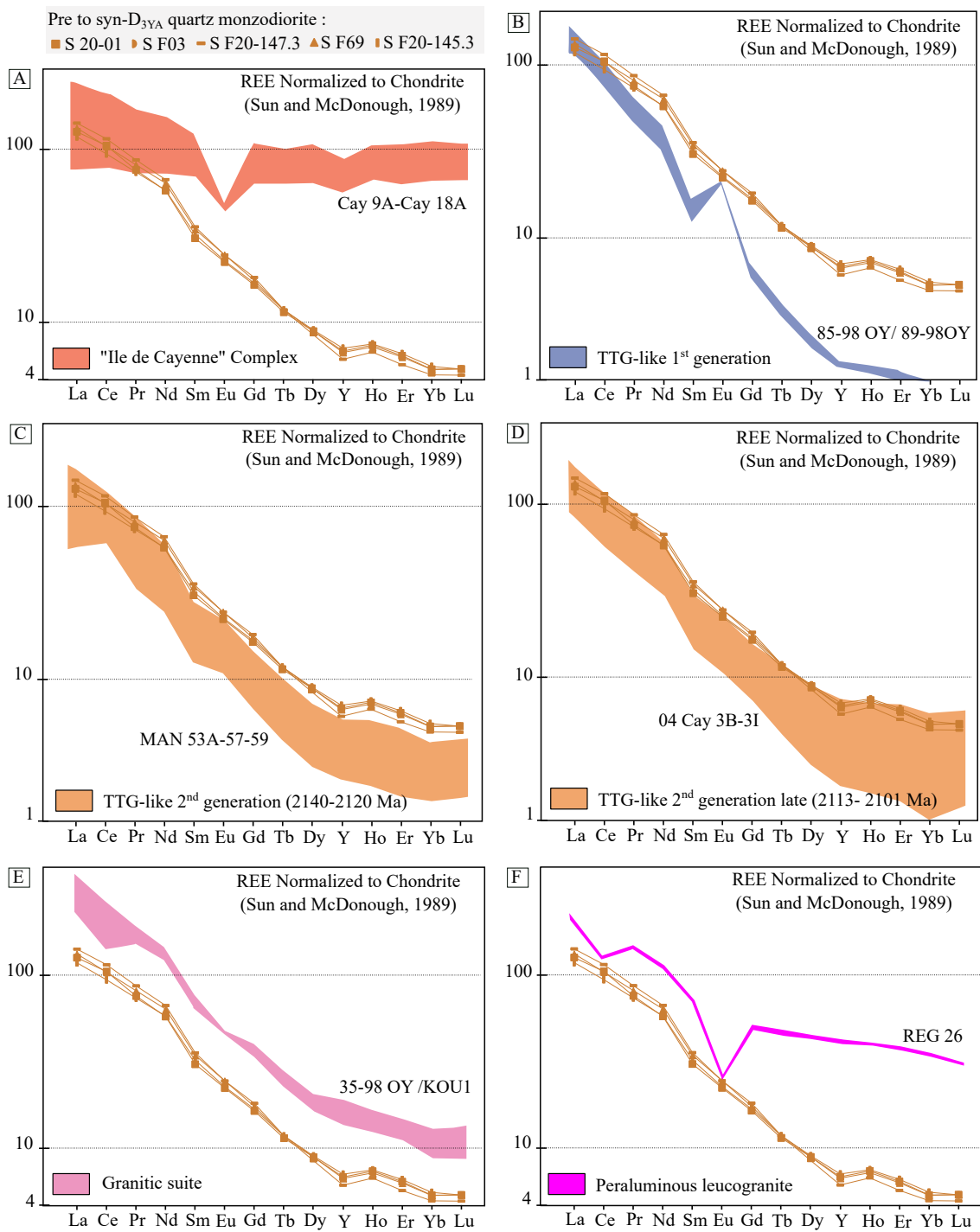


Fig 9 Color, 2-column fitting image.

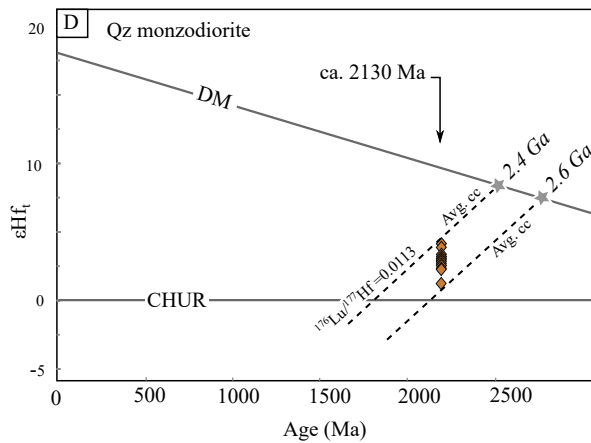
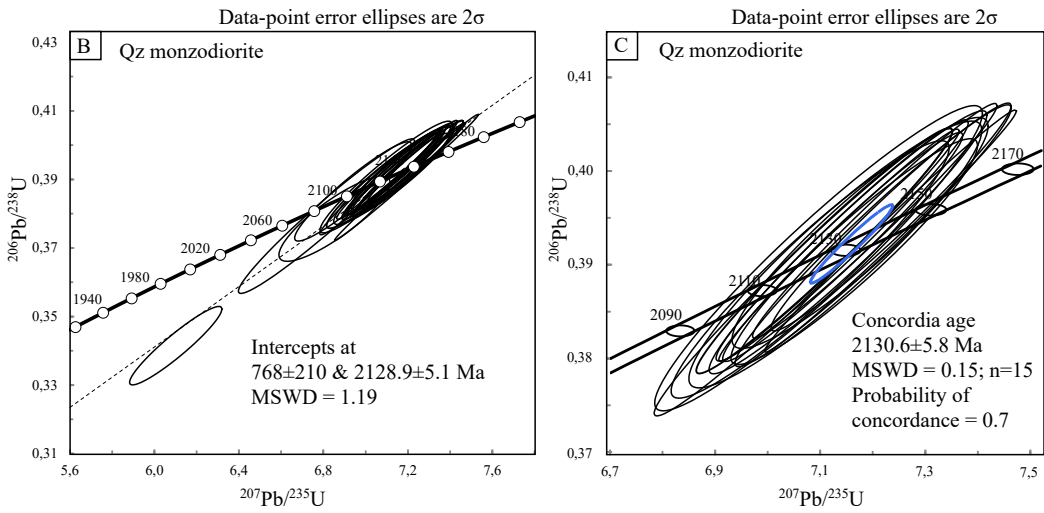
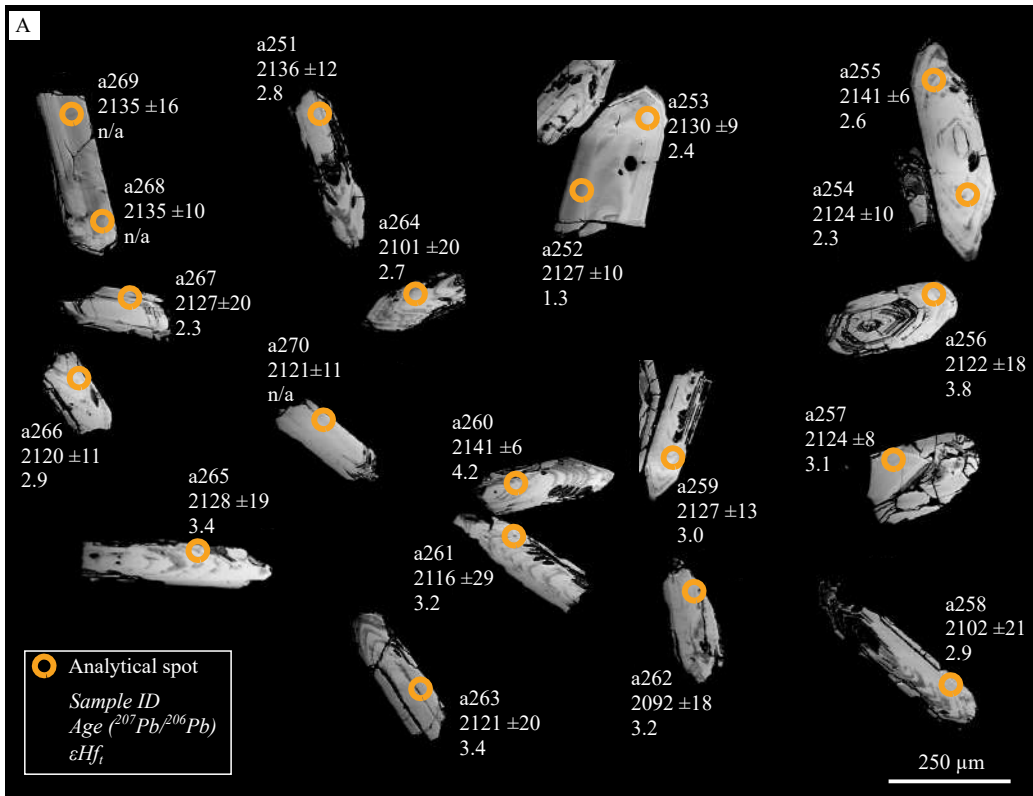


Fig 10 Color, 2-column fitting image.

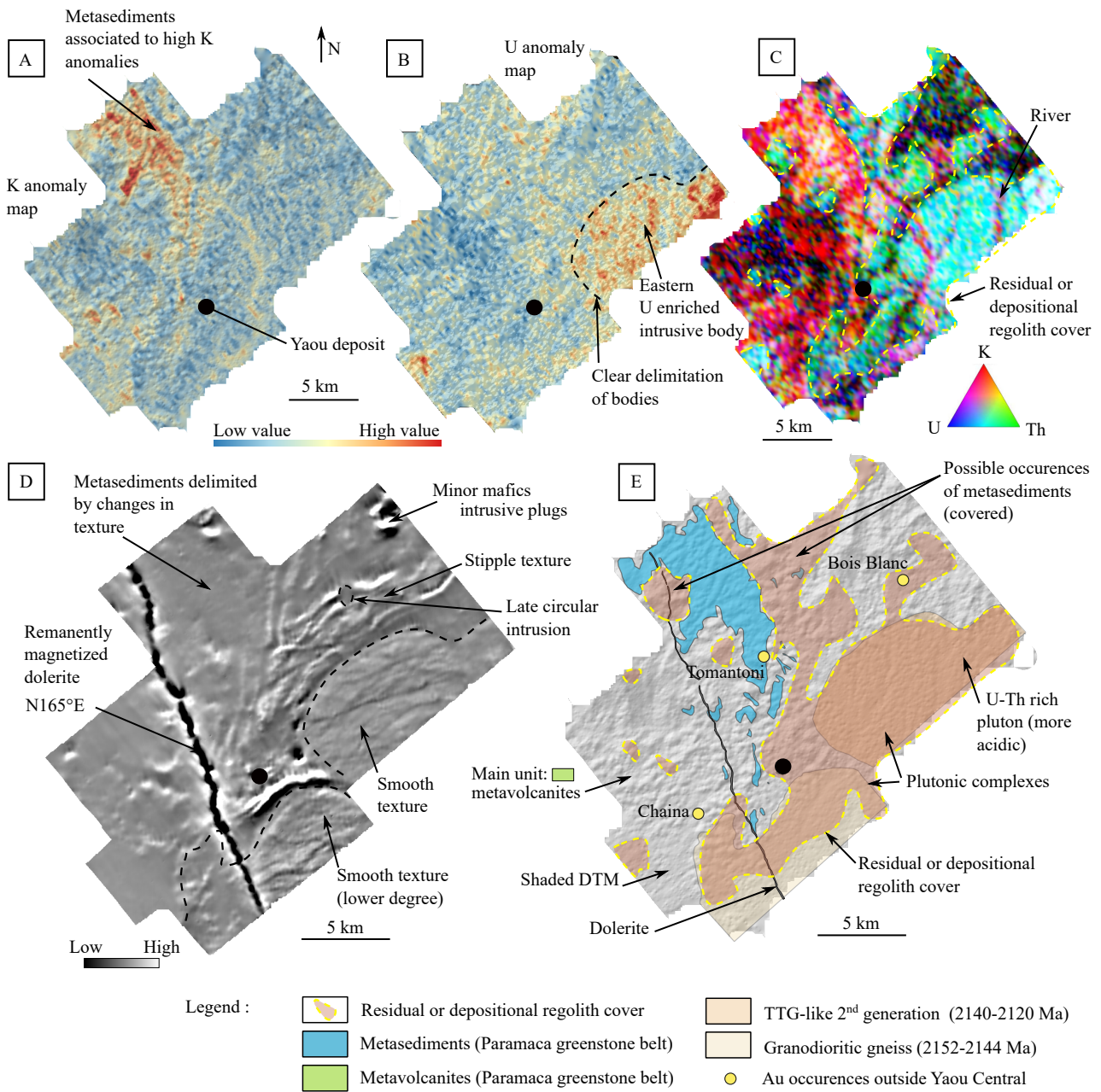


Fig 11 Color, 2-column fitting image.

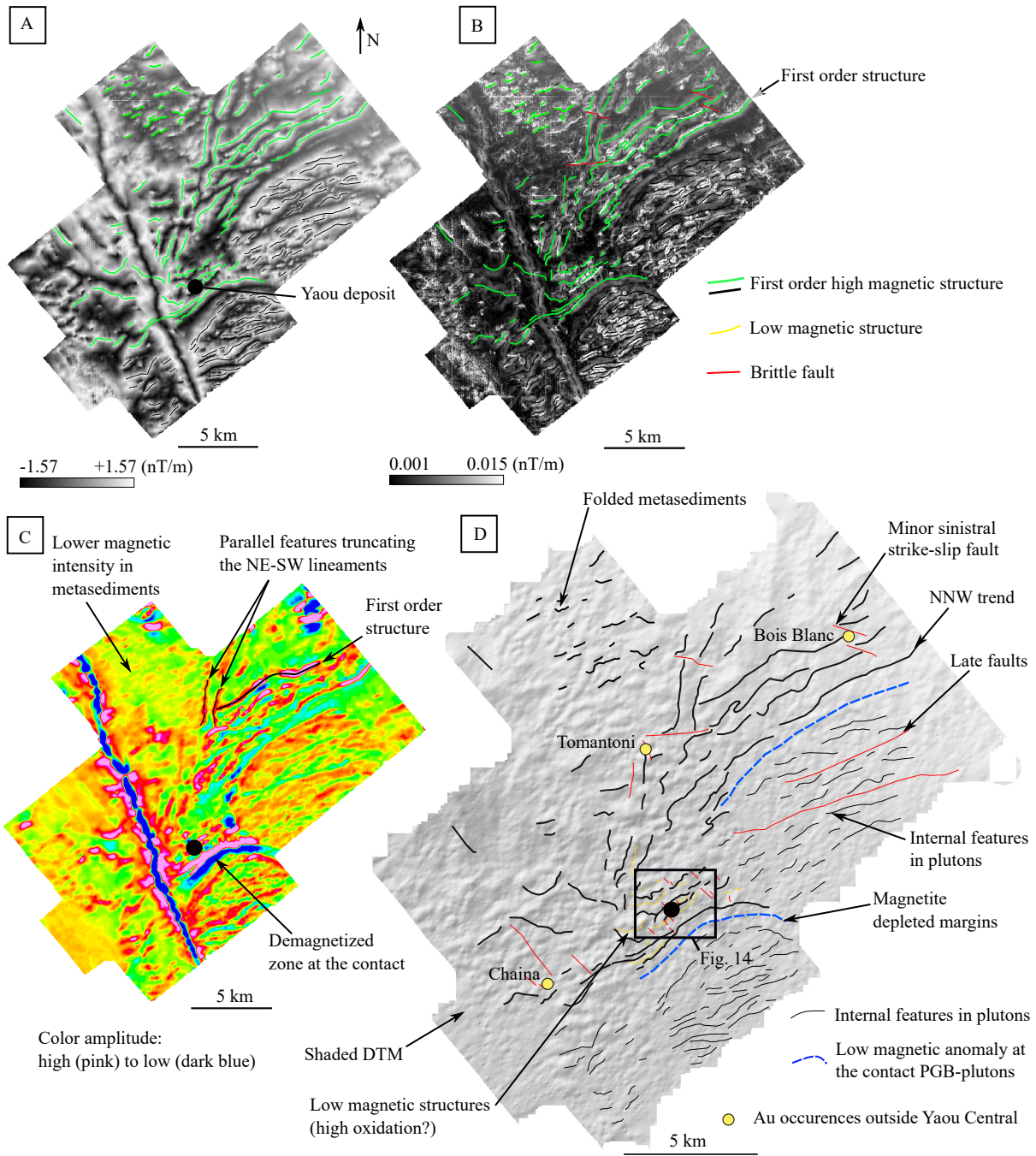


Fig 12 Color, 2-column fitting image.

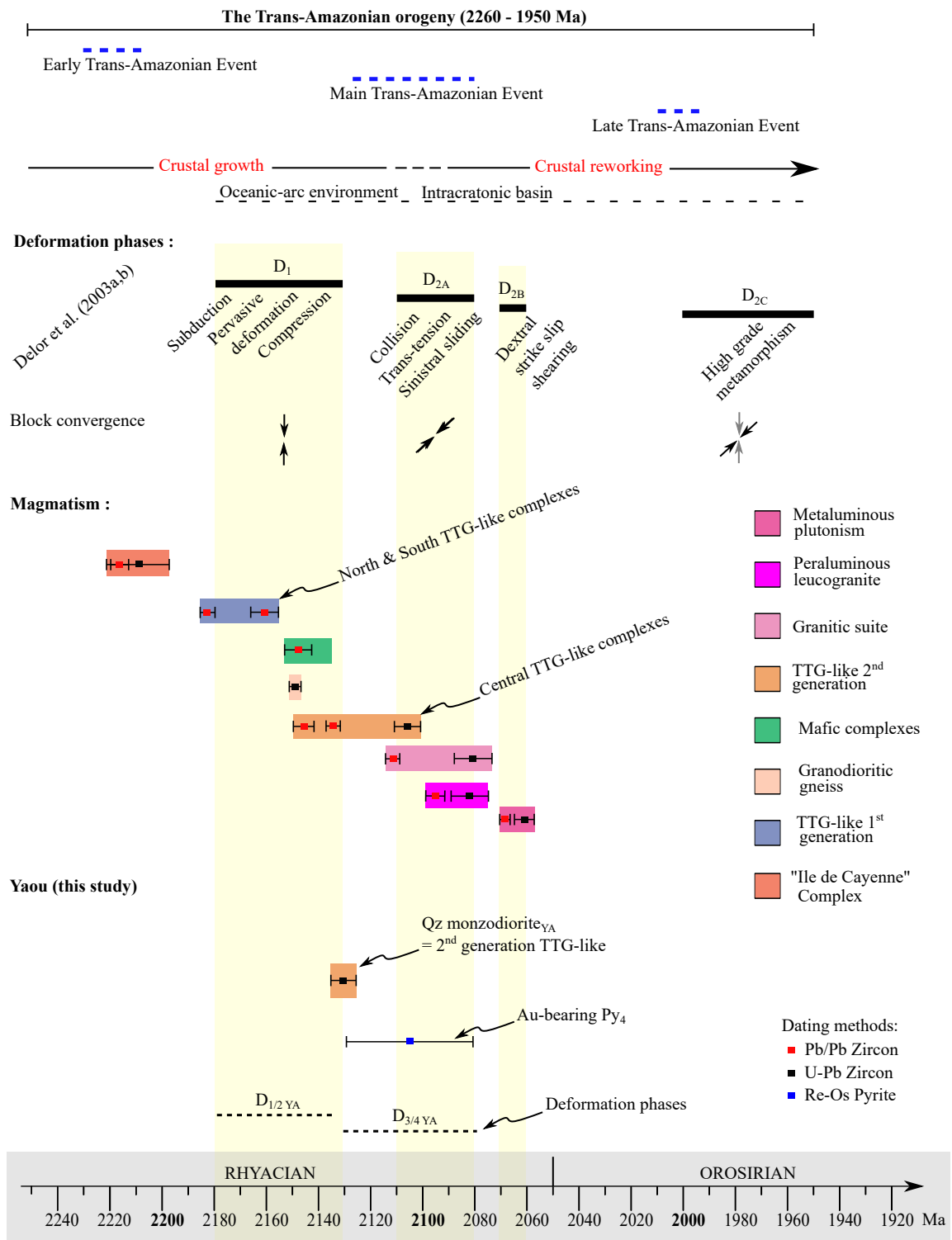


Fig 13 Color, 2-column fitting image.

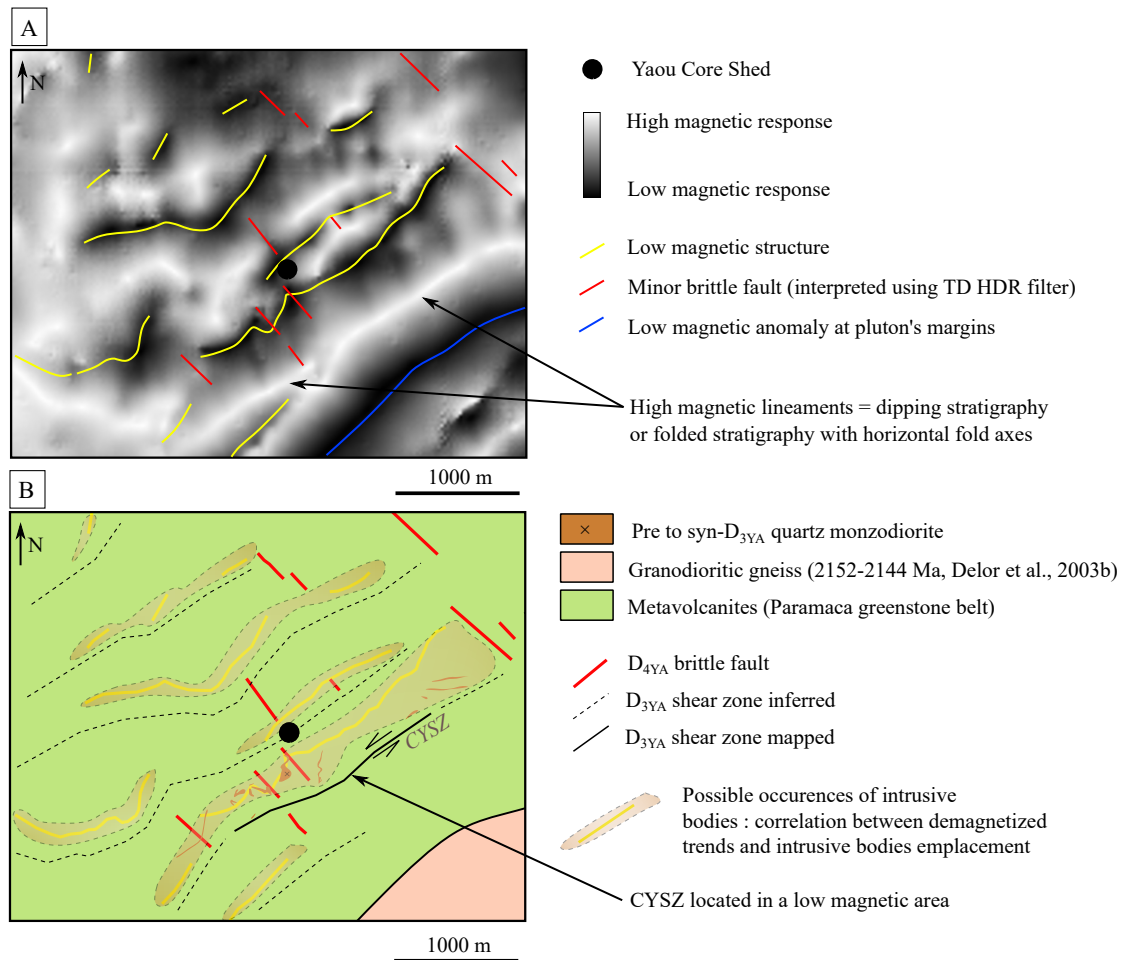


Fig 14 Color, 2-column fitting image.

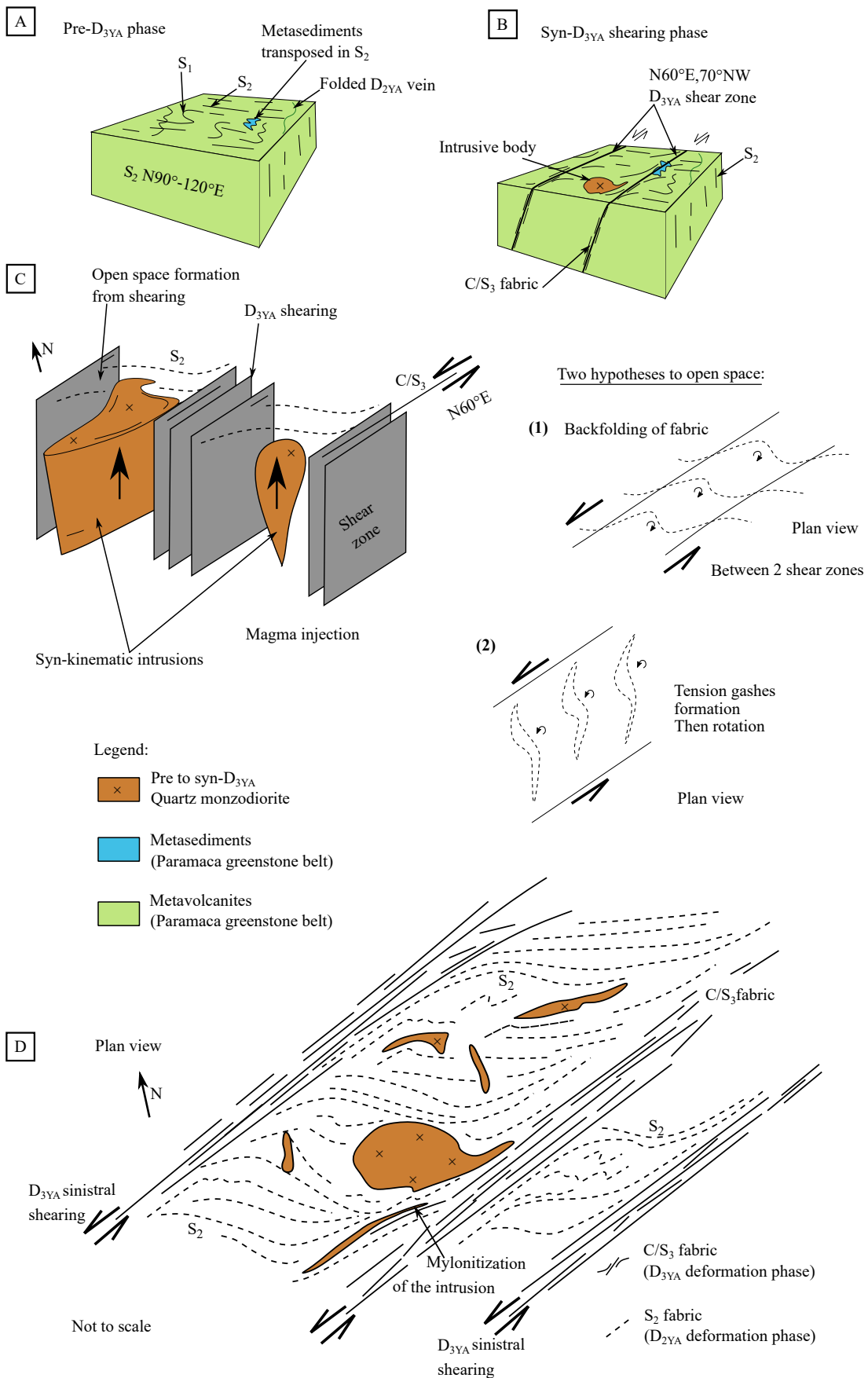


Fig 15 Color, 2-column fitting image.

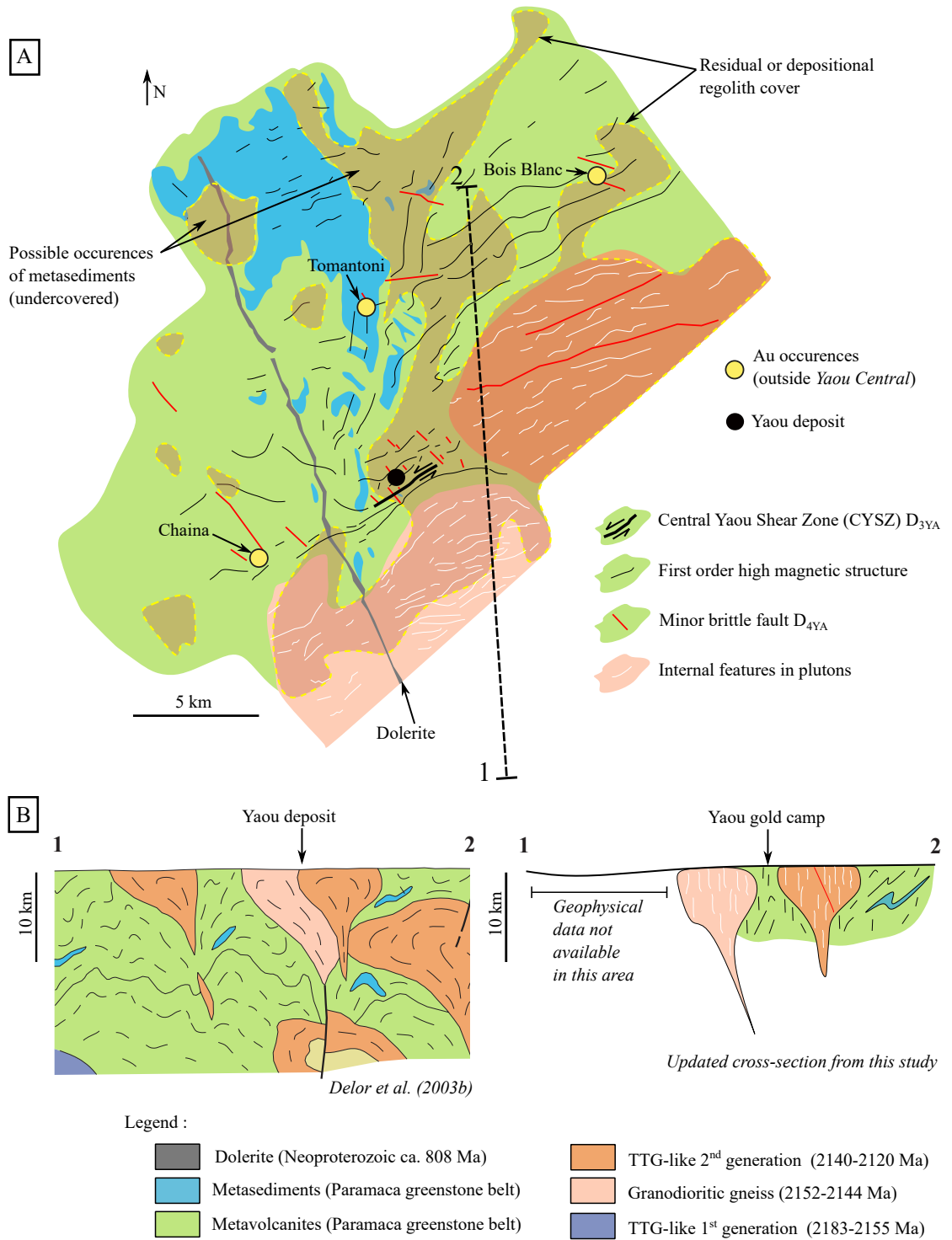


Fig 16 Color, 2-column fitting image.